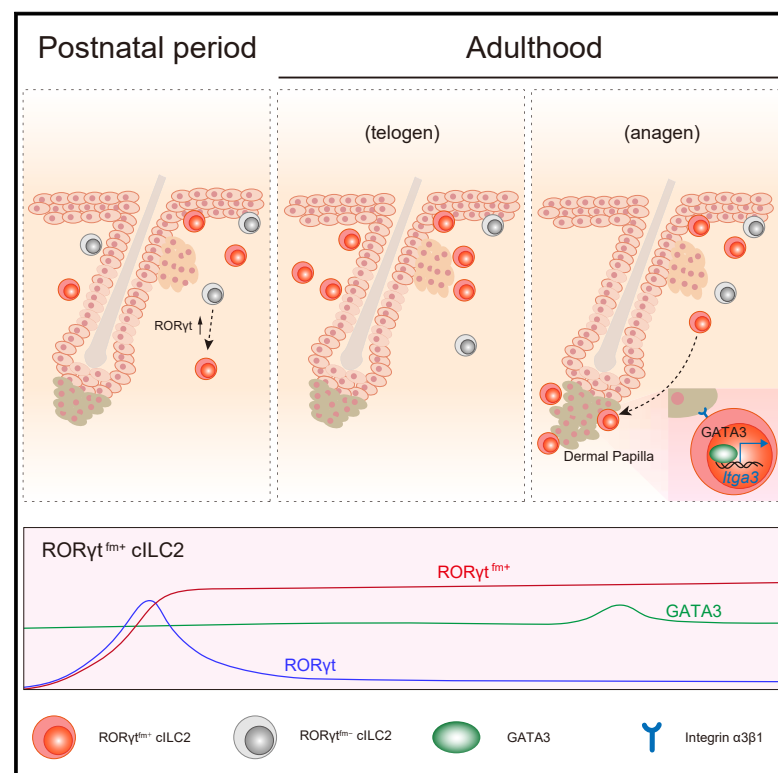# Developmental Cell

Decreased GATA3 levels cause changed mouse cutaneous innate lymphoid cell fate, facilitating hair follicle recycling

Graphical abstract

Authors

Guanqun Ren, Yime Zhang,
Jiamin Liu, ..., Jinfang Zhu, Wenfei Jin,
Chao Zhong

Correspondence

jinwf@sustech.edu.cn (W.J.),
zhongc@pku.edu.cn (C.Z.)

In brief

Cutaneous ILC2s exhibit certain ILC3-like characteristics, yet the underlying mechanism and physiological significance remain elusive. Ren et al. demonstrate that decreased GATA3 levels in them lead to a divergent RORγt fate-mapped subgroup, which accumulates around the hair follicle dermal papilla region through GATA3-controlled integrin α3β1 upregulation, thereby facilitating hair follicle recycling.

Highlights

- Decreased GATA3 levels allow postnatal emergence of RORγt fate-mapped cutaneous ILC2s

- RORγt and GATA3 sequentially promote the terminal divergence of RORγt^{fm+} cILC2s

- RORγt^{fm+} cILC2s accumulate around dermal papilla to facilitate hair follicle recycling

- GATA3-controlled integrin α3β1 expression locates RORγt^{fm+} cILC2s around dermal papilla

CellPress

Developmental Cell

CellPress

Article

Decreased GATA3 levels cause changed mouse cutaneous innate lymphoid cell fate, facilitating hair follicle recycling

Guanqun Ren,[1,2,8] Yime Zhang,[1,2,8] Jiamin Liu,[1,2,8] Wenwen Cheng,[3,8] Di Wu,[1,4,5] Mengwei Han,[1,2] Yanyu Zeng,[1,2] Xingyu Zhao,[1,2] Luni Hu,[1,2] Min Zeng,[1,2] Rama Krishna Gurram,[6] Xiaole Hu,[3] Bo Zhou,[3] Zhiyuan Hou,[2] Jinfang Zhu,[6] Wenfei Jin,[7,*] and Chao Zhong[1,9,*]

[1]Department of Immunology, School of Basic Medical Sciences, NHC Key Laboratory of Medical Immunology, Medicine Innovation Center for Fundamental Researches on Major Immunology-Related Diseases, Peking University, Beijing 100191, China
[2]Institute of Systems Biomedicine, Beijing Key Laboratory of Tumor Systems Biology, Peking University Health Science Center, Beijing 100191, China
[3]Department of Biology, Southern University of Science and Technology, Shenzhen, Guangdong 518055, China
[4]State Key Laboratory of Natural and Biomimetic Drugs, Peking University, Beijing 100191, China
[5]Department of Chemical Biology, School of Pharmaceutical Sciences, Peking University Health Science Center, Beijing 100191, China
[6]Molecular and Cellular Immunoregulation Section, Laboratory of Immune System Biology, National Institute of Allergy and Infectious Diseases, National Institute of Health, Bethesda, MD 20892, USA
[7]CAS Key Laboratory of Computational Biology, Shanghai Institute of Nutrition and Health, Chinese Academy of Sciences, Shanghai, China
[8]These authors contributed equally
[9]Lead contact
*Correspondence: jinwf@sustech.edu.cn (W.J.), zhongc@pku.edu.cn (C.Z.)
https://doi.org/10.1016/j.devcel.2024.04.015

SUMMARY

In mice, skin-resident type 2 innate lymphoid cells (ILC2s) exhibit some ILC3-like characteristics. However, the underlying mechanism remains elusive. Here, we observed lower expression of the ILC2 master regulator GATA3 specifically in cutaneous ILC2s (cILC2s) compared with canonical ILC2s, in line with its functionally divergent role in transcriptional control in cILC2s. Decreased levels of GATA3 enabled the expansion of RORγt fate-mapped (RORγt^{fm+}) cILC2s after postnatal days, displaying certain similarities to ILC3s. Single-cell trajectory analysis showed a sequential promotion of the RORγt^{fm+} cILC2 divergency by RORγt and GATA3. Notably, during hair follicle recycling, these RORγt^{fm+} cILC2s accumulated around the hair follicle dermal papilla (DP) region to facilitate the process. Mechanistically, we found that GATA3-mediated integrin α3β1 upregulation on RORγt^{fm+} cILC2s was required for their positioning around the DP. Overall, our study demonstrates a distinct regulatory role of GATA3 in cILC2s, particularly in promoting the divergence of RORγt^{fm+} cILC2s to facilitate hair follicle recycling.

INTRODUCTION

Innate lymphoid cells (ILCs) are essential components of the immune system.[1–4] Based on their effector functions, ILCs are categorized into type 1 ILCs (ILC1s), which mainly produce interferon (IFN)-γ and tumor necrosis factor alpha (TNF-α), ILC2s prominently secreting interleukin (IL)-5 and IL-13, and ILC3s that primarily release IL-22 and some IL-17. Additionally, there are lymphoid tissue inducer (LTi) cells that share most features with ILC3s but arise from a distinct developmental pathway.[4–6] The development, maintenance, and effector roles of these ILC subsets rely on specific master regulators.[4] Particularly, T-bet is required for ILC1s, GATA3 is essential for ILC2s, and retinoic acid-related orphan receptor gamma t (RORγt) is necessary for both ILC3s and LTi cells.[7–10]

GATA3 is also a critical regulator for the development and functions of all ILCs at multiple stages.[11] Gata3$^{fl/fl}$VavCre mice

exhibit impaired development of all ILCs, highlighting the essential role of GATA3 during ILC development.[9] Furthermore, elevated GATA3 expression determines the lineage specification of ILC1s, ILC2s, and ILC3s from LTi cells.[5,6,12] Once mature, GATA3 remains highly expressed in ILC2s, serving as their master regulator.[8,9] Although the levels of GATA3 are low in ILC3s and LTi cells, it plays a crucial role in promoting their expansion and effector functions.[13]

ILCs play critical roles in maintaining tissue homeostasis.[14] Skin is the outermost and largest barrier tissue of mammals, anatomically consisting of two cutaneous layers, the epidermis and dermis, along with a subcutaneous layer, subcutis.[15] Immune cells play crucial roles in regulating the physiological and pathological processes in skin.[16–18] For example, during hair follicle recycling, regulatory T (Treg) cells expressing Jagged-1 accumulate around the bulge region of hair follicles, promoting efficient activation of hair follicle stem cells and thereby inducing

the anagen phase.[19,20] Skin ILCs have attracted significant interest in recent years.[21–25] They are typically categorized as ILC2s.[21,26–29] Consistently, they display increased IL-5 production during atopic dermatitis, thereby exacerbating the disease.[26,28,30,31] However, they also possess certain alternative characteristics. A subgroup of skin ILCs located near sebaceous glands constrains sebaceous hyperplasia through secreting TNF and lymphotoxin.[22] Additionally, skin ILCs are found to adopt a pathogenic ILC3-like state during psoriasis.[23] However, the mechanism underlying these unique traits of skin ILCs remains unclear.

RESULTS

cILC2s exhibit decreased GATA3 expression

Similar to other ILC subsets, skin ILCs lacked markers for mature hematopoietic lineages, while expressing CD90, CD127, and Id2 (Figures S1A and S1B). They were absent in $Rag2^{-/-}Il2rg^{-/-}$ mice (Figure S1C). In each mouse ear, they numbered approximately 2,000, constituting ~5% of immune cells (Figure S1D). Skin ILCs were missing in $Gata3^{fl/fl}VavCre$ mice, indicating their origin from common ILC progenitors (Figure S1E).[6] Across various skin layers, they were primarily distributed in the dermis, with comparatively lower presence in the epidermis and subcutis in terms of both percentages and numbers (Figures S1F and S1G). Skin ILCs did not express the master regulators T-bet and RORγt associated with ILC1 and ILC3, and thus were typically categorized as ILC2s (Figure S1H).[21,32,33] However, they showed a capacity to converge toward a pathogenic ILC3-like state during psoriasis.[23]

To elucidate the distinction of skin ILCs from canonical ILC2s, the ILC2 master regulator GATA3 was particularly examined utilizing a $Gata3$ reporter mice tool ($Gata3^{ZsG-fl/fl}$) (Figures 1A and S1I).[34] In epidermal and dermal layers, skin ILCs exhibited lower GATA3-ZsG levels than those in subcutaneous layer (Figures 1B and 1C). The subcutaneous ILCs and small intestine lamina propria (siLP) ILC2s showed equivalent GATA3-ZsG levels. Whereas, although GATA3-ZsG levels in epidermal and dermal ILCs decreased, they remained higher than in other ILC subsets (Figure 1D). Further, only ILCs from epidermis and dermis showed decreased GATA3-ZsG levels among ILC2s from different tissues, largely excluding the contribution of tissue environment to the change (Figure 1E). Consistently, the decrease in endogenous GATA3 expression in epidermal and dermal ILCs was verified by anti-GATA3 staining (Figures 1F and 1G). These findings suggested that ILCs in the two cutaneous layers, hereafter referred to as cutaneous ILC2s (cILC2s), differed from canonical ILC2s, including those in the subcutis. Based on an assay for transposase-accessible chromatin with high-throughput sequencing (ATAC-seq) analysis, cILC2s exhibited reduced chromatin accessibility at the $Gata3$ locus compared with canonical ILC2s, suggesting potential cell-intrinsic alterations contributing to the decrease in GATA3 expression (Figure 1H).[35]

We further conducted a single-cell RNA sequencing (scRNA-seq) analysis on ILCs from skin and small intestine, distinguished by different Sample Tags (Figure S1J). These cells were classified into cILC2, ILC1, ILC2, ILC3, and LTi based on their signature genes (Figures S1K and S1L). ILCs from skin and small

intestine were further confirmed using Sample Tags (Figure S1M). Consistent with the variations in GATA3 levels, cILC2s and siLP ILC2s were separated into distinct clusters, highlighting significant differences in their transcriptomes (Figure S1K). Thus, the top 20 differentially expressed genes between cILC2s and siLP ILC2s were profiled (Figure S1N). Interestingly, $Il18r1$ and $Itgae$ (encoding CD103) were upregulated in cILC2s, while $Klrg1$ (encoding killer cell lectin like receptor G1, or KLRG1) was specifically expressed by siLP ILC2s. A previous study on lung ILC2s categorized the IL-18R1$^+$CD103$^+$ subgroup with decreased GATA3 expression as immature ILC2s, while ST2$^+$KLRG1$^+$ ILC2s were considered as effector cells.[33] However, cILC2s exhibited notable expression of IL-18R1 and CD103, along with considerable expression of ST2 and minimal expression of KLRG1 (Figure S1O). Additionally, around 20% of cILC2s had expressed IL-5 (IL-5^{fm+}) according to IL-5 fate mapping, indicating their classification as effector cells (Figure S1P). Nevertheless, both IL-5^{fm+} and IL-5^{fm-} cILC2s showed similar expression of IL-18R1, CD103, ST2, and KLRG1 (Figure S1Q). Thus, further exploration of the relationship between cILC2s and immature ILC2s in the lung is still required. Finally, almost no cILC2s had expressed IL-22, eliminating the possibility of ILC3 contamination in our analysis (Figure S1R).

Together, these findings suggest a significant decrease in GATA3 expression in cILC2s compared with canonical ILC2s, indicating the potential presence of distinct characteristics.

GATA3 exerts a unique transcriptional regulatory role in cILC2s

Given the dosage effect of GATA3-mediated transcriptional regulation,[36] we wondered whether GATA3 played distinct roles in cILC2s compared with canonical ILC2s. Thus, a $Gata3^{ZsG-fl/fl}$ CreER^{T2} mouse strain enabling transient $Gata3$ deletion ($Gata3^{ZsG-KO}$) through tamoxifen administration was developed (Figures 2A and 2B). The $Gata3$ deletion efficiency was confirmed by absence of siLP ILC2s and subcutaneous ILC2s (Figures S2A and S2B). However, cILC2s remained unaffected (Figures 2B and 2C). $Gata3$ deficiency also led to a reduction in ILC3 and LTi cells due to decreased CD127 expression,[13] but the CD127 levels and number of cILC2s remained stable following $Gata3$ deletion (Figure 2D). Moreover, the GATA3-ZsG levels in $Gata3^{ZsG-KO}$ and $Gata3^{ZsG-fl/fl}$ cILC2s were comparable, suggesting that GATA3 did not promote its own expression in cILC2s (Figure 2E). Further, $Gata3$ deletion was performed in vitro on canonical siLP ILC2s and cILC2s isolated from $Gata3^{ZsG-fl/fl}$CreER^{T2} mice through 4-hydroxytamoxifen (4-OHT) administration (Figures 2F and S2C). Consistently, siLP ILC2 number decreased progressively, accompanied by decreased GATA3-ZsG levels after 2 days (Figures S2D and S2E). By contrast, the number and GATA3-ZsG levels of cILC2 remained unchanged, indicating distinct regulatory roles of GATA3 in cILC2s (Figures 2G and 2H). We thus conducted an RNA sequencing (RNA-seq) analysis on sort-purified cILC2s from tamoxifen-administered $Gata3^{fl/fl}$ and $Gata3^{fl/fl}$-CreER^{T2} ($Gata3^{KO}$) mice (Figure 2I). Consequently, 267 GATA3-upregulated and 169 GATA3-downregulated genes (transcripts per kilobase million [TPM] > 5, fold change > 2, and $p < 0.05$) were identified (Figure 2J). Among the GATA3-upregulated genes were well-known effector genes of canonical ILC2s, like $Il5$, $Il13$, $Areg$, $Calca$, and $Il1rl1$. However, GATA3 also enhanced
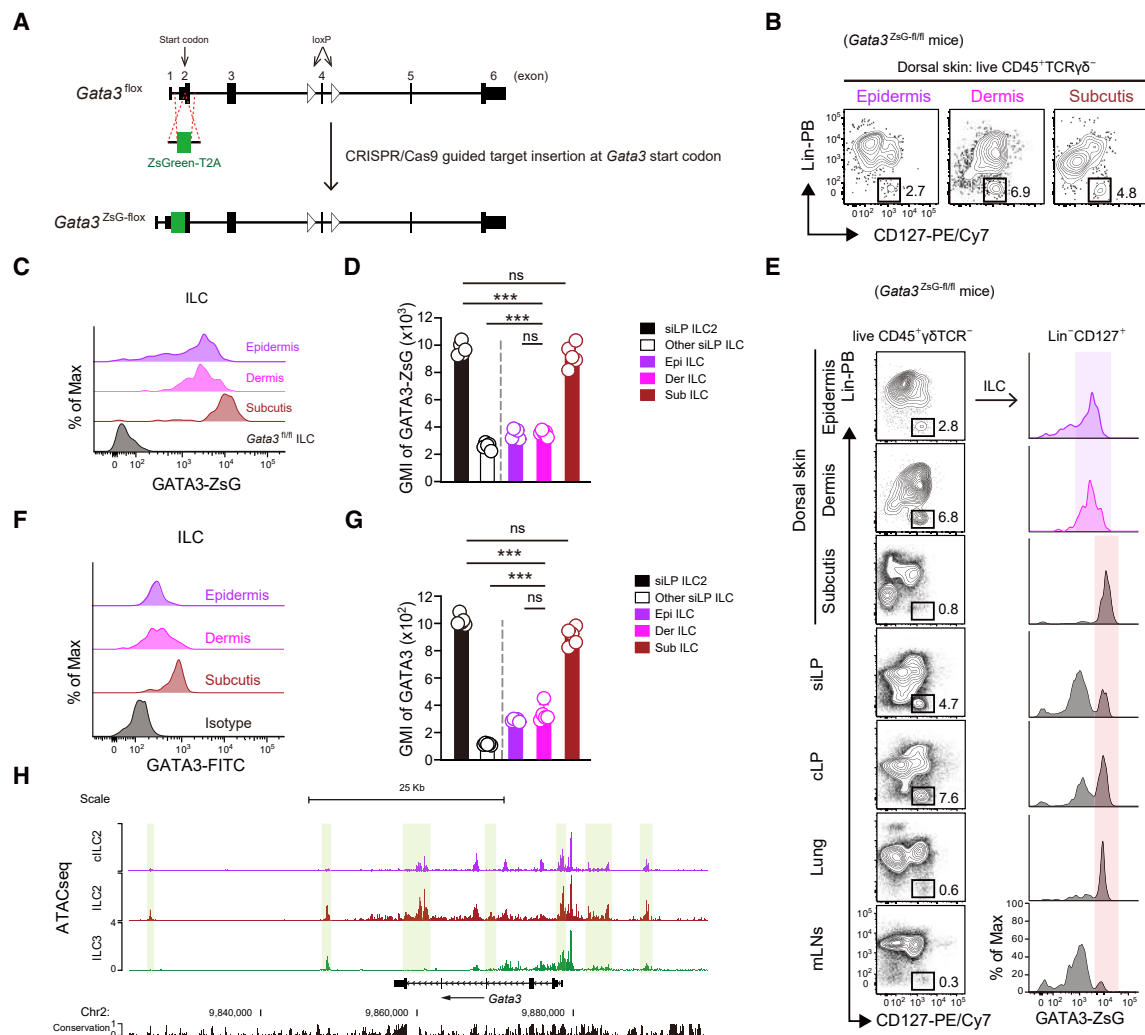
Figure 1. GATA3 exhibits decreased expression in cILC2s

(A) Construction strategy for *Gata3*$^{ZsG-fl/fl}$ mice.

(B) Representative flow cytometry showing ILCs in epidermis (Epi), dermis (Der), and subcutis (Sub) of dorsal skin. Lineage (Lin) markers include CD3e, CD5, CD19, B220, CD11b, CD11c, NK1.1, FcεRI, TER-119, and Gr-1.

(C) Representative histogram showing GATA3-ZsG levels in ILCs from epidermis, dermis, and subcutis.

(D) Comparison of GATA3-ZsG levels in ILC subsets of the indicated tissues (*n* = 5 per group).

(E) Representative flow cytometry showing GATA3-ZsG levels in ILC2s of the indicated tissues.

(F) Representative histogram showing GATA3 levels in ILCs from epidermis, dermis, and subcutis.

(G) Comparison of GATA3 expression in ILC subsets of the indicated tissues (*n* = 5 per group).

(H) Chromatin accessibility at *Gata3* locus in cILC2s, canonical ILC2s and ILC3s (GSE77695).

Numbers indicate the percentages in each gate. Data are shown as mean ± SEM. *p* values are calculated by unpaired t test. ns, not significant, ***$p < 0.001$. Data are representative of at least three independent experiments.

See also Figure S1.

Il17a expression in cILC2s, and its deficiency resulted in upregulated *Il1r1*, *Il23r*, and *Il6ra*, indicating that the decreased GATA3 levels might confer some ILC3-like features to cILC2s. Additionally, GATA3 upregulated several noncanonical effector genes in cILC2s, including *S100a8*. These findings underscore the distinct regulatory role of GATA3 in cILC2s compared with canonical ILC2s.

Further, the regulatory effects of GATA3 across all ILC subsets were examined leveraging publicly available RNA-seq data (GSE47851 and GSE71198) (Figure S2F).[9,13] Comparative anal-

ysis revealed distinct sets of GATA3-regulated and -downregulated genes in cILC2s, ILC2s, ILC3s, and LTi cells (Figures 2K, 2L, and S2G). Particularly, only a small fraction of the GATA3-regulated genes exhibited similar expression patterns between cILC2 and canonical ILC2s, ILC3s, or LTi cells, emphasizing the distinct regulatory role of GATA3 in cILC2s (Figures 2L and S2H). In addition, while the GATA3 binding motif was identified in opening chromatin regions (OCRs) associated with ~60% of the GATA3-upregulated genes in canonical ILC2s, this percentage decreased to ~40% in cILC2s, as well as in ILC3s and LTi
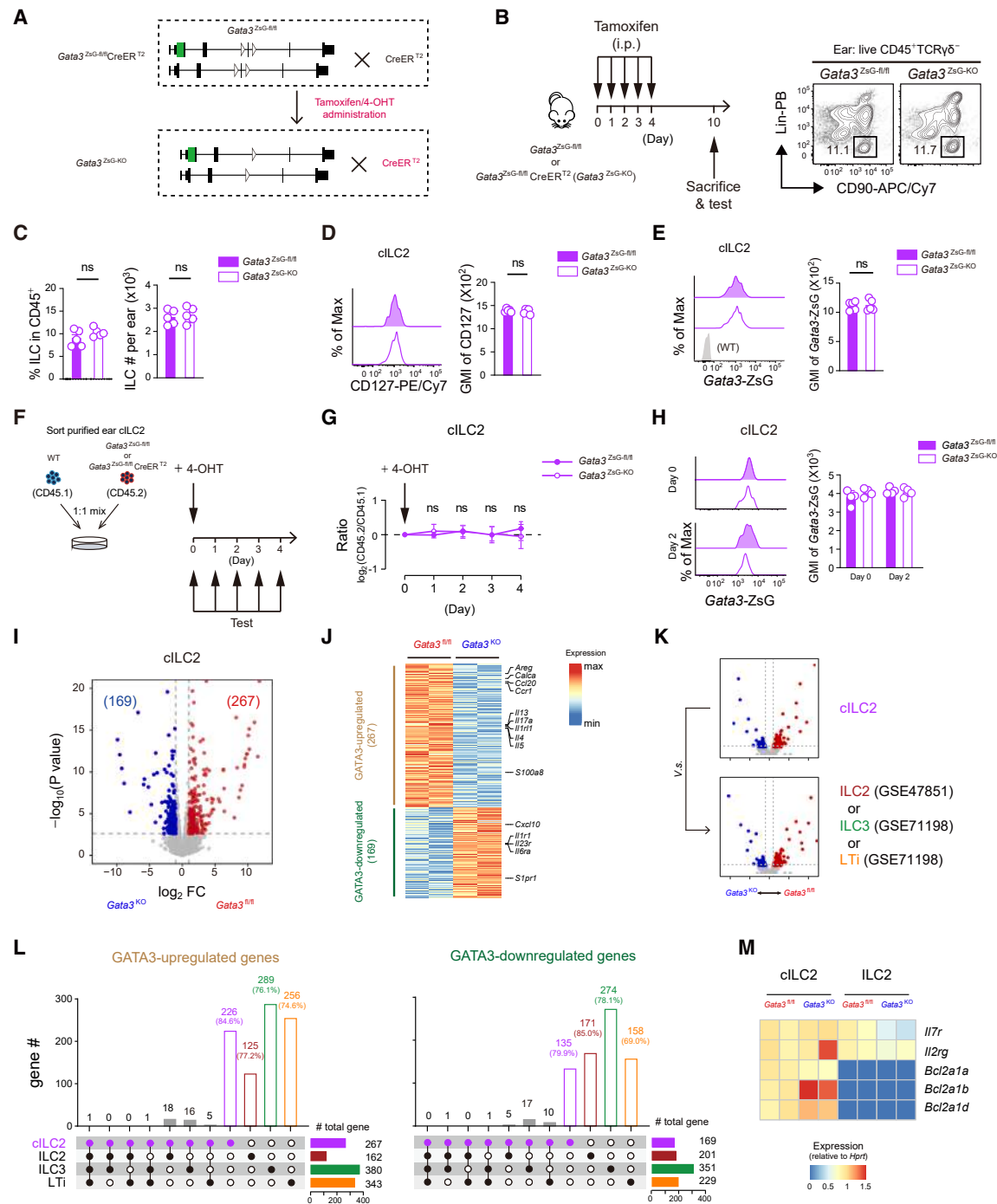
Figure 2. GATA3 exerts a unique regulatory role in cILC2s

(A) Construction strategy for $Gata3^{ZsG-fl/fl}$CreER^{T2} mice and $Gata3^{ZsG-KO}$ mice.

(B) Schematic diagram illustrating tamoxifen administration on $Gata3^{ZsG-fl/fl}$ and $Gata3^{ZsG-KO}$ mice (left) and representative flow cytometry of cILC2s in the ears (right).

(C) Percentages and numbers of ear cILC2s in $Gata3^{ZsG-fl/fl}$ and $Gata3^{ZsG-KO}$ mice ($n = 5$ per group).

(D) Representative histogram showing CD127 expression on ear cILC2s from $Gata3^{ZsG-fl/fl}$ and $Gata3^{ZsG-KO}$ mice (left) and geometric mean fluorescence intensity (GMI) of CD127 levels ($n = 5$ per group) (right).

(E) Representative histogram showing GATA3-ZsG expression in ear cILC2s from $Gata3^{ZsG-fl/fl}$ and $Gata3^{ZsG-KO}$ mice (left) and GMI of GATA3-ZsG levels ($n = 5$ per group) (right). GATA3-ZsG expression in wild-type (WT) ear cILC2s is used as negative control.

(F) Schematics of deleting $Gata3$ in sort-purified ear cILC2s from $Gata3^{ZsG-fl/fl}$ or $Gata3^{ZsG-fl/fl}$CreER^{T2} (CD45.2) mice and congenic (CD45.1) mice.

(G) Dynamic ratio changes between CD45.2 and CD45.1 cILC2s in (F) ($n = 4$ per group).

Developmental Cell
Article

CellPress

cells, further indicating a disparity in GATA3-mediated transcriptional regulation between cILC2s and canonical ILC2s (Figures S2I and S2J). Notably, while the levels of *Il7r* remained unaffected in *Gata3*[KO] cILC2s, they significantly reduced in *Gata3*[KO] canonical ILC2s (Figure 2M). Additionally, cILC2s displayed specific expression of anti-apoptotic gene *Bcl2a1*, including *Bcl2a1a*, *Bcl2a1b*, and *Bcl2a1d* (Figures 2M and S2K),[37,38] and two of these isoforms, *Bcl2a1b* and *Bcl2a1d*, were upregulated in *Gata3*[KO] cILC2s, potentially contributing to the survival of cILC2s after *Gata3* deletion (Figure 2M).

Collectively, GATA3 is not indispensable for the maintenance of cILC2s and exerts regulatory effects over a specific set of genes, underscoring its distinctive regulatory function in cILC2s.

Decreased GATA3 levels associate with the divergence of RORγt[fm+] cILC2s

Consistent with the *Il17a* expression, ∼75% of cILC2s had undergone RORγt expression (RORγt[fm+]), as demonstrated by RORγt fate mapping (*Rosa26*[Tdtomato]*Rorc*-Cre, or *Rorc*-fm) (Figure 3A). By contrast, the proportions of RORγt[fm+] canonical ILC2s in the subcutis, siLP, or lung were all below 10% (Figure 3B). RORγt[fm+] and RORγt[fm−] cILC2s displayed similar expression of IL-18R1, CD103, ST2, and KLRG1 (Figure S3A). However, RORγt[fm+] cILC2s exhibited subtle RORγt expression compared with RORγt[fm−] cILC2s (Figure 3C). Additionally, RORγt[fm−] cILC2s did not acquire RORγt expression when traced in transferred *Gata3*^{fl/fl}*Vav*Cre recipients, eliminating the emergence of RORγt[fm+] cILC2s from RORγt[fm−] cILC2s during adulthood (Figure 3D). Thus, RORγt expression in cILC2s was examined in newborn mice. The percentage of RORγt[fm+] cILC2s was only 20% on postnatal day 10 (P10) but rapidly rose to ∼55% by P14 (Figure 3E). Consistently, RORγt expression in cILC2s peaked on P14 compared with P10 and adulthood (Figure 3F). Thus, the postnatal emergence of RORγt[fm+] cILC2s, along with increased RORγt expression, suggested a divergence process for cILC2s.

Through transcriptomic comparison between RORγt[fm+] and RORγt[fm−] cILC2s using RNA-seq, we identified 241 and 324 upregulated genes (TPM > 5, fold change > 2, and *p* < 0.05) in them, respectively (Figure 3G; Table S1). Among the upregulated genes in RORγt[fm+] cILC2s were *Rorc*, *Il17f*, and *Lta*, indicating that they might possess some ILC3-like characteristics. Correspondingly, upon stimulation, RORγt[fm+] cILC2s, rather than RORγt[fm−] cILC2s, demonstrated IL-17A production (Figure 3H). By contrast, the upregulated genes in RORγt[fm−] cILC2s included *Il4*, *Il5*, *Areg*, and *Il1rl1*, indicating a closer resemblance to canonical ILC2s (Figure 3G). Consistently, upon stimulation, they produced more IL-5 than RORγt[fm+] cILC2s (Figure S3B). An

empiric cumulative distribution function (ECDF) plot also illustrated the preferential expression of the RORγt[fm+] cILC2-upregulated genes within ILC3s over canonical ILC2s (Figure S3C). Further, through ATAC-seq analysis, there were 1,463 RORγt[fm+] cILC2-specific OCRs shared with either canonical ILC2s or ILC3s displaying preferentially increased accessibility in ILC3s, while 1,538 RORγt[fm−] cILC2-specific OCRs tending to show enhanced accessibility in canonical ILC2s (Figure S3D). Specifically, RORγt[fm+] cILC2s showed increased accessibility to the *Il17a* and *Il17f* loci while reducing accessibility to the *Il5* locus (Figure S3E). Overall, these findings indicate that RORγt[fm+] cILC2s share greater similarity with ILC3s in terms of both transcriptome and chromatin accessibility.

GATA3 expression further decreased in RORγt[fm+] cILC2s, raising the possibility of its involvement in their divergency (Figure 3I). Thus, the transcriptomic differences between *Gata3*^{fl/fl} and *Gata3*[KO] cILC2s were compared with those between RORγt[fm+] and RORγt[fm−] cILC2s (Figures 2I and 3G). An ECDF plot showed that the RORγt[fm−] cILC2-upregulated genes were also preferentially expressed in *Gata3*^{fl/fl} cILC2s (Figure 3J). Specifically, *Areg*, *Il4*, *Il5*, *Il13*, and *Il1rl1* were downregulated in both RORγt[fm+] cILC2s and *Gata3*[KO] cILC2s, suggesting that the decreased GATA3 expression might be correlated with the divergence of RORγt[fm+] cILC2s (Figure 3K). Additionally, the involvement of RORγt in this process was also evaluated. *Rorc* deficiency (*Rorc*^{fl/fl}*Vav*Cre, or *Rorc*[KO] in brief) did not impact the development or maintenance of cILC2s, further excluding their origin from ILC3s (Figure S3F). Nevertheless, transcriptomic change in *Rorc*[KO] cILC2s were observed, suggesting that RORγt indeed left certain imprints in RORγt[fm+] cILC2s, despite being shortly expressed postnatally (Figure S3G). However, the ECDF plot indicated that RORγt was not involved in the divergence of RORγt[fm+] cILC2s (Figure S3H).

Altogether, these data indicate that the transient postnatal RORγt expression leads to the emergence of a distinct RORγt[fm+] cILC2 subgroup with certain ILC3-like characteristics, and the decreased GATA3 levels in cILC2s are associated with this divergency.

RORγt and GATA3 sequentially promote the divergence of RORγt[fm+] cILC2s

To further elucidate the regulatory roles of RORγt and GATA3 in cILC2s, a scRNA-seq analysis was conducted on cILC2s from wild-type (WT), *Rorc*[KO], and *Gata3*[KO] mice in their adulthood (Figures 4A and S4A). After integrating with the previous WT cILC2 scRNA-seq data (Figures S1J and S1K), these cILC2s were further classified into 6 clusters, namely *Tnf*+, *Cxcr4*+, *Jmy*+, *Ccr6*+, *Areg*+, and *Il1rl1*+, based on their preferentially

---

(H) Representative histogram showing GATA3-ZsG expression in *Gata3*[ZsG-fl/fl] and *Gata3*[ZsG-KO] cILC2s on days 0 and 2 post 4-OHT treatment (left), and GMI of GATA3-ZsG levels (*n* = 4 per group) (right).

(I) Volcano plot depicting gene expression difference between ear cILC2s of tamoxifen-treated *Gata3*^{fl/fl} and *Gata3*^{fl/fl}CreER[T2] (*Gata3*[KO]) mice (TPM > 5, fold change > 2, and *p* < 0.05).

(J) Heatmap profiling the differential genes between *Gata3*^{fl/fl} and *Gata3*[KO] cILC2s.

(K) Schematics showing comparison of GATA3-regulated genes in cILC2s and canonical ILC2s (GSE47851), ILC3s, or LTi cells (GSE71198).

(L) UpSet plot showing shared or unique GATA3-regulated genes across the indicated ILC subsets.

(M) Relative expression of the indicated genes in cILC2s and canonical ILC2s from *Gata3*^{fl/fl} and *Gata3*[KO] mice (GSE47851).

Numbers indicate the percentages in each gate. Data are shown as mean ± SEM. *p* values are calculated by unpaired t test. ns, not significant. Data are representative of at least three independent experiments.

See also Figure S2.

Figure 3. GATA3 negatively correlates with divergency of RORγt^fm+ cILC2s

(A) Representative flow cytometry showing RORγt fate mapping of cILC2s.

(B) Representative histogram showing RORγt fate mapping of ILC2s from the indicated tissues (left) and percentages of the RORγt^fm+ cells (*n* = 6 per group) (right).

(C) Representative histogram showing RORγt expression in RORγt^fm+ and RORγt^fm− cILC2s (left), and GMI of RORγt levels (*n* = 4 per group) (right).

(D) Schematics of transferring RORγt^fm+ or RORγt^fm− cILC2s to irradiated *Gata3*^fl/fl^*Vav*Cre recipient mice (left), representative flow cytometry showing RORγt fate mapping of the transferred cILC2s after 4–6 weeks (middle), and percentages of the RORγt^fm+ cells (*n* = 5 per group) (right).

(E) Representative flow cytometry showing RORγt fate mapping of cILC2s at postnatal day 10 (P10), P14, and adulthood (>6 weeks) (left), and percentages of the RORγt^fm+ cells (*n* = 3 per group) (right).

(F) Representative flow cytometry showing RORγt expression in cILC2s at P10, P14, and adulthood (>6 weeks) (left) and percentages of the RORγt^+ cells (*n* = 5 per group) (right).

(G) Volcano plot depicting gene expression difference between RORγt^fm+ and RORγt^fm− cILC2s (TPM > 5, fold change > 2, and *p* < 0.05).

(H) Representative flow cytometry showing IL-17A production in RORγt^fm+ and RORγt^fm− cILC2s after stimulated with PMA and ionomycin for 3 h (left), and percentages of the IL-17A^+ cells (*n* = 5 per group) (right).

(I) Representative histogram comparing GATA3 expression between RORγt^fm+ and RORγt^fm− cILC2s (left), and GMI of the GATA3 levels (*n* = 4 per group) (right).

(legend continued on next page)

Developmental Cell
Article

CellPress

expressed genes (Figures 4B, S4B, and S4C). All 6 clusters exhibited significant expression of *Gata3* and were not contaminated by ILC1s, ILC3s, or T cells (Figure S4D). Among them, the *Areg*+ and *Il1rl1*+ clusters demonstrated obvious RORγt^fm− cILC2 features characterized by the expression of their upregulated genes, while the *Jmy*+ and *Ccr6*+ clusters exhibited typical RORγt^fm+ cILC2 traits (Figures 4C and S4E). Additionally, the *Tnf*+ and *Cxcr4*+ clusters, while not clearly demonstrating RORγt^fm+ cILC2 features, already showed diminished RORγt^fm− cILC2 characteristics, indicating that they were in the early stages of RORγt^fm+ cILC2 divergence. This observation was further supported by profiling the RORγt^fm+ and RORγt^fm− cILC2-upregulated genes across the 6 clusters (Figure S4F). Next, cILC2s from WT, *Gata3*^KO, and *Rorc*^KO mice were individually examined (Figures 4D and S4G). No significant alterations were found in *Gata3*^KO or *Rorc*^KO cILC2s regarding the expression of effector cytokines for ILC3s and ILC2s, such as *Il17a*, *Il5*, *Il13*, *Csf2*, and *Areg*, as well as markers for immature lung ILC2s, like *Il18r1* and *Itgae* (Figure S4H). However, using a Milo tool,[39] we did observe that the percentage of RORγt^fm− cILC2 clusters significantly decreased in *Gata3*^KO mice, but almost remained unchanged in *Rorc*^KO mice, confirming the impact of GATA3 on the RORγt^fm+ cILC2 divergency (Figures 4D, 4E, and S4I). Additionally, through a particular examination of the RORγt^fm+ cILC2s, a notable increase in the percentage of the *Tnf*+ cluster was observed in *Rorc*^KO cILC2s, while a significant increase in the percentage of the *Jmy*+ cluster was identified in *Gata3*^KO cILC2s, suggesting that RORγt and GATA3 sequentially promoted the further divergence of RORγt^fm+ cILC2s toward the terminal stage (Figure 4F).

A pseudotime trajectory analysis was further performed. The RORγt^fm+ cILC2s followed a divergency path starting from the *Tnf*+ cluster, passing through the *Cxcr4*+ and *Jmy*+ clusters, and ending at the *Ccr6*+ cluster, while the RORγt^fm− cILC2s followed a progression from the *Areg*+ cluster to the *Il1rl1*+ cluster (Figure S4J). The influence of RORγt and GATA3 on the RORγt^fm+ cILC2 divergency was further explored by assessing the difference between individual trajectories in WT, *Gata3*^KO, and *Rorc*^KO cILC2s (Figure 4G). Consistently, RORγt primarily dictated the divergence of RORγt^fm+ cILC2s at an early stage, while GATA3 promoted the divergency in the later stage (Figure 4H). Based on cell density along the pseudotime trajectory, we divided the RORγt^fm+ cILC2 into four divergence stages, roughly corresponding to the 4 clusters. Gene modules for the four divergence stages were defined validated by their expression dynamics along the trajectory (Figure 4I). We found that progression of the *Cxcr4*+ cluster from stage I to stage II was delayed by *Rorc* deficiency, while advancement of the *Ccr6*+ cluster from stage III to stage IV was impeded by *Gata3* deficiency (Figure 4J). Further, using a mouse strain with specific *Gata3* deficiency in RORγt^fm+ cILC2s (*Rosa26*^Tdtomato *Gata3*^fl/fl*Rorc*-Cre, or *Rorc*-fm^ΔGata3), the impaired terminal

divergence of RORγt^fm+ cILC2s was confirmed as indicated by their significantly reduced CCR6 expression (Figures 4K, S4K, and S4L). By contrast, the CCR6 levels in cILC2s of *Rorc*^KO mice remained unchanged (Figure 4L).

Collectively, the scRNA-seq analysis suggests that RORγt and GATA3 sequentially regulate the divergence of RORγt^fm+ cILC2s, promoting them to a final stage with enhanced CCR6 expression.

RORγt^fm+ cILC2s is crucial in regulating hair follicle recycling

Despite the acknowledged role of cILC2s during pathology, their involvement in physiological processes in the skin remained largely unexplored.[22–25] During postnatal days, cILC2s rapidly expanded from P7 to P10, coinciding with the onset of hair growth, which raised the possibility that cILC2s might participate in this process (Figures S5A and S5B). Thus, a depilation-induced synchronized hair regrowth model, previously used to elucidate the role of Treg cells in hair follicle recycling, was employed to evaluate the hair regrowth differences among WT mice, *Rag2*^−/− mice lacking T cells, and *Gata3*^fl/fl*Vav*Cre mice with further cILC2s absence in the skin.[19] Consistent with our expectation, *Gata3*^fl/fl*Vav*Cre mice displayed significantly delayed hair regrowth compared with both WT and *Rag2*^−/− mice (Figures 5A and 5B). Further, reconstitution of *Gata3*^fl/fl*Vav*Cre mice with cILC2s and T cells led to notably accelerated hair regrowth compared with the reconstitution with T cells alone, suggesting a difference between the roles of cILC2s and Treg cells in this process (Figures 5C, 5D, and S5C–S5I). In addition, the reconstitution with cILC2s alone also accelerated hair regrowth in *Gata3*^fl/fl*Vav*Cre mice (Figure S5J). Together, these findings suggest that cILC2s facilitate hair follicle recycling.

The number of cILC2s remained unchanged throughout depilation-induced hair regrowth (Figure S5K). Thus, to further elucidate the alterations in cILC2 during this process, we conducted a scRNA-seq analysis on cILC2s from different time points of depilation-induced hair regrowth (Figures 5E and S5L). These cells were projected onto the previously obtained cILC2 uniform manifold approximation and projection (UMAP) plot, and the absence of contamination by T cells or other ILCs was validated (Figures S5M–S5O). The cILC2s at different time points were subsequently divided using their Sample Tags (Figure S5P). Proportional analysis of the cILC2 clusters revealed a notable increase in the *Ccr6*+ cluster on day 7 (Figure 5F). Consistently, upregulated CCR6 levels on cILC2s were observed then, indicated that RORγt^fm+ cILC2s might contribute to hair follicle recycling (Figure 5G). Indeed, reconstitution of *Gata3*^fl/fl*Vav*Cre mice with RORγt^fm+ cILC2s and T cells led to enhanced hair regrowth compared with the reconstitution with RORγt^fm− cILC2s and T cells, or T cells alone (Figures 5H and S5Q). Additionally, the interaction between cILC2s and hair follicle cells was explored. Hair follicle cells, enriched via cell sorting, underwent scRNA-seq and classification analyses (Figure S5R). Using a CellChat

---

(J) Empirical cumulative distribution function (ECDF) plot showing relative expression of genes upregulated in RORγt^fm+ (yellow line) and RORγt^fm− (red line) cILC2s in comparison with the gene expression difference between *Gata3*^fl/fl and *Gata3*^KO cILC2s. Whole genes were used as a reference (gray line).

(K) Heatmap showing expression difference of the indicated genes between RORγt^fm+ and RORγt^fm− cILC2s, as well as between *Gata3*^fl/fl and *Gata3*^KO cILC2s.

Numbers indicate the percentages in each gate. Data are shown as mean ± SEM. *p* values are calculated by unpaired t test. ns, not significant, *$p < 0.05$, **$p < 0.01$, ***$p < 0.001$. Data are representative of at least three independent experiments (A–C, E, F, H, and I) and two independent experiments (D, G, J, and K). See also Figure S3 and Table S1.
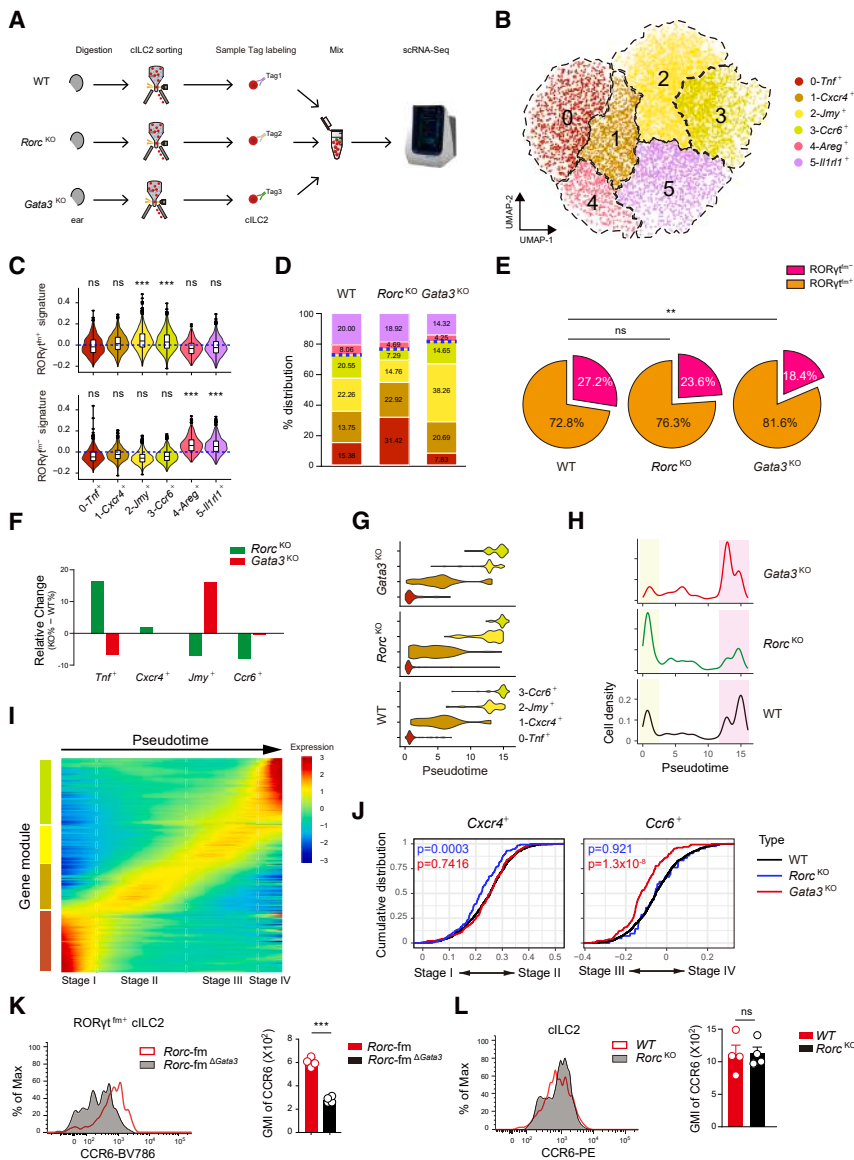
Figure 4. RORγt and GATA3 sequentially promote the divergency of RORγt^fm+ cILC2s

(A) Schematics of scRNA-seq analysis on cILC2s from WT, *Rorc*^KO, and *Gata3*^KO mice.

(B) UMAP showing cILC2 classification.

(C) Violin plots showing the RORγt^fm+ and RORγt^fm− cILC2 features (related to Figure 3G) in each cILC2 cluster. *p* values were calculated by Mann-Whitney U test between each cluster and other clusters.

(D) Individual distribution of the cILC2 clusters in WT, *Rorc*^KO, and *Gata3*^KO mice.

(E) Pie chart showing percentages of cILC2 clusters referring to RORγt^fm+ and RORγt^fm− cILC2s in WT, *Rorc*^KO, and *Gata3*^KO mice. The percentages were calculated with the Milo tool, and *p* values were calculated by Mann-Whitney U test.

(F) Bar chart showing percentage changes of RORγt^fm+ cILC2 clusters in *Rorc*^KO (green bar) and *Gata3*^KO (red bar) mice compared with WT mice.

(G) Distribution of the four RORγt^fm+ cILC2 clusters in WT, *Rorc*^KO, and *Gata3*^KO mice alongside the pseudotime trajectory (related to Figure S4J).

(H) Density of RORγt^fm+ cILC2s along the pseudo-time trajectory in WT, *Rorc*^KO, and *Gata3*^KO mice.

(I) Division of RORγt^fm+ cILC2s into four divergence stages based on gene expression dynamics alongside the pseudotime trajectory.

(J) ECDF plot showing relative expression of the genes annotated to *Cxcr4*^+ (left) and *Ccr6*^+ (right) cILC2 clusters in *Rorc*^KO (blue line), *Gata3*^KO (red line), and WT (black line) mice, in comparison with the gene expression difference between stages I and II (left), and between stages III and IV (right).

(K) Representative flow cytometry showing CCR6 expression on RORγt^fm+ cILC2s from *Rorc*-fm and *Rorc*-fm^ΔGata3 mice (left), and GMI of the CCR6 levels (*n* = 4 per group) (right).

(L) Representative flow cytometry showing CCR6 expression on cILC2s from *Rorc*^fl/fl and *Rorc*^KO mice (left), and GMI of the CCR6 levels (*n* = 4 per group) (right).

Data are shown as mean ± SEM. *p* values are calculated by unpaired t test. ns, not significant, ***p* < 0.001. Data are representative of two independent experiments (B–J) and at least three independent experiments (K and L).

See also Figure S4.

algorithm, we discovered that *Ccr6*^+ cILC2s exhibited preferential interaction with dermal papilla (DP) cells, which were known to provide essential signals for hair regrowth, as well as to a less extent with hair follicle cells (Figure 5I). Consistently, we observed a significant accumulation of RORγt^fm+ cILC2s around the hair follicle DP region on day 7 post-depilation, accompanied by a decrease in their distribution around the infundibulum (IF) region (Figures 5J, 5K, S5S, and S5T). Therefore, our data suggest that RORγt^fm+ cILC2s are essential in facilitating hair follicle recycling.

RORγt^fm+ cILC2s facilitate hair follicle recycling through GATA3

The *Ccr6*^+ cILC2 cluster that showed a proportional increase on day 7 post-depilation displayed elevated expression of *Ostf1*, *Fgl2*, as well as several S100 molecules (*S100a4*, *S100a6*, *S100a10*, and *S100a11*), while the prior *Jmy*^+ cluster exhibited

relatively lower levels of these genes (Figures 6A and S6A). Whereas, in line with inhibitory roles of type 2 cytokines such as including IL-5 and IL-13 on hair follicle stem cell proliferation and hair regrowth,[25] the expression of *Il5* and *Il13* decreased in the *Ccr6*^+ cluster on day 7 (Figure 6A). Additionally, an intensified divergence of *Ccr6*^+ cILC2s from stage III to stage IV was observed on day 7 post-depilation (Figure 6B). Consistent with the role of GATA3 in the late-stage divergency, both its expression and regulatory activity, as indicated by the upregulation of its target genes, increased on day 7, implicating that the role of RORγt^fm+ cILC2s in hair follicle recycling was regulated by GATA3 (Figures 6C and S6B). Indeed, comparing the depilation-induced hair regrowth between *Rorc*-fm and *Rorc*-fm^ΔGata3 mice showed that *Gata3* deficiency resulted in substantially impeded hair regrowth (Figures 6D and S6C). Moreover, although RORγt^fm+ cILC2s showed sustained numbers in *Rorc*-fm^ΔGata3 mice, their CCR6 levels were markedly
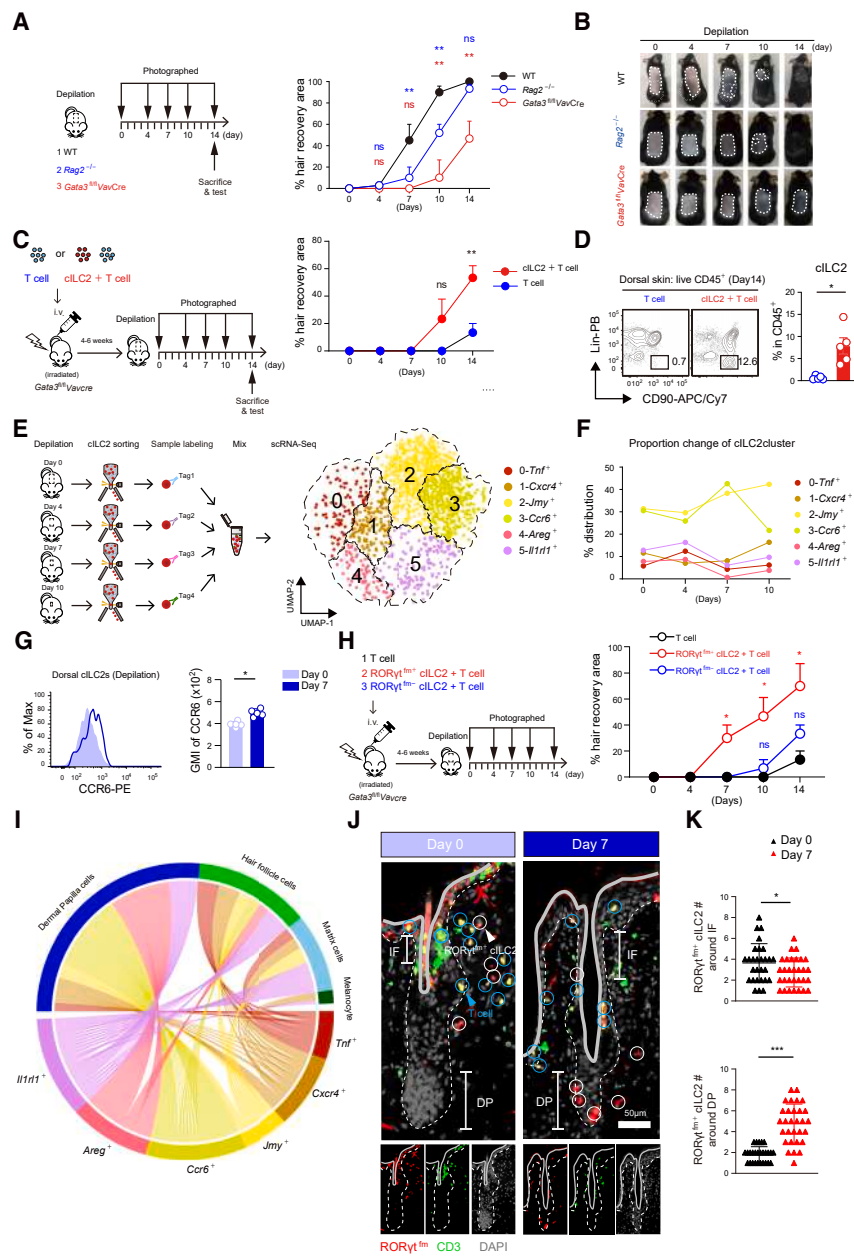
Developmental Cell
Article

Figure 5. RORγt^fm+ cILC2s facilitate hair follicle recycling

(A) Schematics of depilation-induced hair regrowth (left) and the kinetics in WT, *Rag2^−/−*, and *Gata3^fl/fl VavCre* mice (*n* = 4 per group) (right).

(B) Representative photographs showing hair regrowth in WT, *Rag2^−/−*, and *Gata3^fl/fl VavCre* mice.

(C) Schematics of depilation-induced hair regrowth in *Gata3^fl/fl VavCre* mice reconstituted by cILC2s and T cells or T cells alone (left), and the kinetics (*n* = 4 per group) (right).

(D) Representative flow cytometry showing replenish of cILC2s in dorsal skin of *Gata3^fl/fl VavCre* mice reconstituted by cILC2s and T cells or T cells alone (left), and percentages of the reconstituted cILC2s in CD45^+ immune cells (*n* = 5 per group) (right).

(E) Schematics of scRNA-seq on cILC2s across different time points of depilation-induced hair regrowth (left), and UMAP visualization of cILC2 clusters projected onto the previous plot (Figure 4B) (right).

(F) Proportion change of cILC2 clusters along depilation-induced hair regrowth.

(G) Representative histogram showing CCR6 expression on dorsal skin cILC2s at days 0 and 7 post depilation (left), and GMI of the CCR6 levels (*n* = 5 per group) (right).

(H) Schematics of depilation-induced hair regrowth in *Gata3^fl/fl VavCre* mice reconstituted by RORγt^fm+ cILC2s and T cells, RORγt^fm− cILC2s and T cells, or T cells alone (left), and the kinetics (*n* = 5 per group) (right).

(I) Cell-cell communication between cILC2s and hair follicle cells inferred using CellChat.

(J) Representative confocal image showing positioning of RORγt^fm+ cILC2s around hair follicles on day 0 (left) and day 7 of depilation-induced hair regrowth (right).

(K) Numbers of RORγt^fm+ cILC2s around infundibulum (IF) (*n* = 28 and 30) (top) and dermal papilla (DP) region of hair follicles (bottom) on days 0 and 7 of depilation-induced hair regrowth (*n* = 27 and 30). Each dot represents the cell number around a single follicle (<20 μm).

Numbers indicate the percentages in each gate. Data are shown as mean ± SEM. *p* values are calculated by unpaired *t* test. ns, not significant, **p* < 0.05, ***p* < 0.01, ****p* < 0.001. Data are representative of at least three independent experiments (A–D, G, H, J, and K) and two independent experiments (E, F, and I).

See also Figure S5.

diminished, indicating that their terminal divergence was critical for hair follicle recycling (Figures 6E and S6D). Additionally, we observed disrupted accumulation of RORγt^fm+ cILC2s surrounding the hair follicle DP region on day 7 post-depilation, highlighting the importance of GATA3 in directing the positioning process (Figures 6F and 6G). To further exclude potential interference by T cell defects in the *Rorc*-fm^ΔGata3 mice, we also performed the depilation-induced hair regrowth on *Gata3^fl/fl VavCre* mice reconstituted by RORγt^fm+ cILC2s from either *Rorc*-fm or *Rorc*-fm^ΔGata3 mice and WT T cells (Figure 6H). Consistently, RORγt^fm+ cILC2s from *Rorc*-fm^ΔGata3 mice could not effectively restore the hair regrowth (Figures 6H and S6E). And their CCR6 levels remained low after reconstitution (Figure S6F).

Altogether, these findings highlight the fundamental role of GATA3 during hair follicle recycling, which promotes the final divergence of RORγt^fm+ cILC2s and their positioning around the hair follicle DP region.

GATA3 regulates RORγt^fm+ cILC2 positioning by promoting integrin α3β1 expression

Next, the underlying mechanism of GATA3-regulated RORγt^fm+ cILC2 positioning during hair follicle recycling was explored through a screening for genes upregulated by GATA3 both on day 7 post-depilation and in the *Ccr6^+* cILC2 cluster (Figures S7A and S7B). Ultimately, only *Itga3* (encoding integrin α3), which associated with cell adhesion, was identified (Figure S7C). Notably, *Itgb1* (encoding integrin β1) that formed a

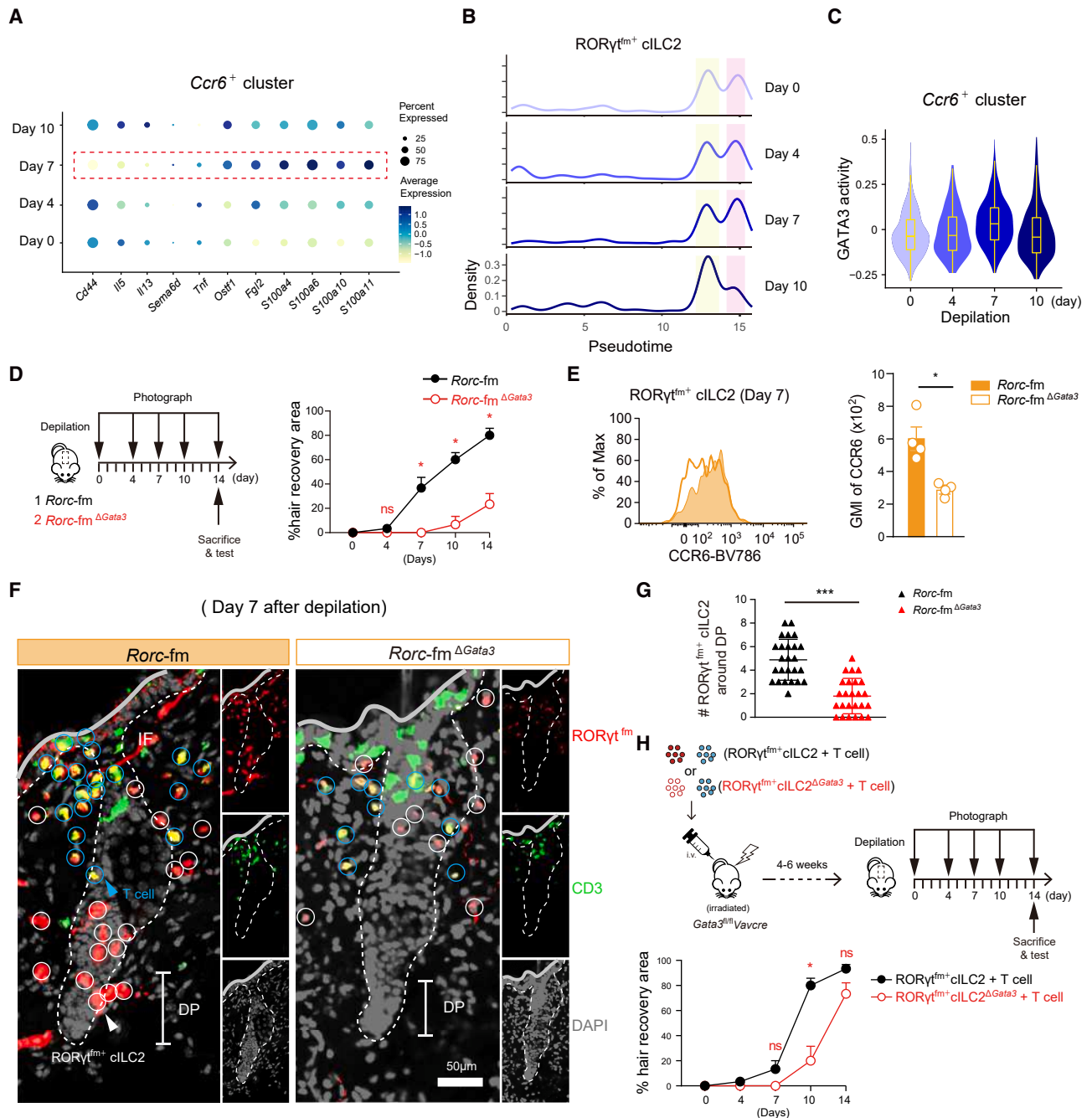**Figure 6. RORγt^fm+ cILC2s require GATA3 to facilitate hair follicle recycling**

(A) Bubble plot showing expression of the indicated effector genes in the *Ccr6+* cILC2 cluster during depilation-induced hair regrowth.

(B) Density changes of RORγt^fm+ cILC2s along their pseudotime trajectory (related to Figure S4J) during depilation-induced hair regrowth.

(C) Violin plot evaluating GATA3-upregulated genes (related to Figure 2I) in the *Ccr6+* cILC2 cluster during depilation-induced hair regrowth.

(D) Schematics of depilation-induced hair regrowth in *Rorc*-fm and *Rorc*-fm^ΔGata3 mice (left), and the kinetics ($n = 4$ per group) (right).

(E) Representative histogram showing CCR6 expression on RORγt^fm+ cILC2s from dorsal skin of *Rorc*-fm or *Rorc*-fm^ΔGata3 mice on day 7 post-depilation (left), and GMI of the CCR6 levels ($n = 4$ per group) (right).

(F) Representative confocal image showing positioning of RORγt^fm+ cILC2s around hair follicles in *Rorc*-fm (left) or *Rorc*-fm^ΔGata3 (right) mice on day 7 of depilation-induced hair regrowth.

(G) Numbers of RORγt^fm+ cILC2s around hair follicle DP region in *Rorc*-fm and *Rorc*-fm^ΔGata3 mice on day 7 post-depilation ($n = 25$ per group). Each dot represents the number of cells around a single follicle (<20 μm).

(legend continued on next page)

Developmental Cell
Article

CellPress

dimer with *Itga3* was also found to be upregulated on day 7 post-depilation (Figure 7A). The increase in integrin α3β1 levels on RORγt^{fm+} cILC2s during hair follicle recycling was further validated by flow cytometry (Figure S7D). Consistently, the DP and hair follicle cells that interacted with *Ccr6$^+$* cILC2s also exhibited preferential expression of the laminin receptors for this integrin, including *Lama3*, *Lamb3*, *Lamc2* (forming Laminin-332), *Lama5*, *Lamb1*, and *Lamc1* (forming Laminin-511) (Figure S7E).[40–42] Most importantly, the upregulation of integrin α3β1 was disrupted on RORγt^{fm+} cILC2s of *Rorc*-fm^{ΔGata3} mice (Figure 7B). To further assess the direct regulation by GATA3, we revisited previous anti-GATA3 chromatin immuno-precipitation (ChIP)-seq data on ILC2s and identified a GATA3 binding site within the relevant OCRs of *Itga3* in cILC2s (Figure 7C). Through CUT&RUN-qPCR, we confirmed that the GATA binding also existed in cILC2s specifically on day 7 post-depilation (Figure 7D). Thus, GATA3 directly regulates the expression of *Itga3* in RORγt^{fm+} cILC2s during hair follicle recycling.

To further elucidate the role of integrin α3β1 in positioning RORγt^{fm+} cILC2s, an integrin α3β1 inhibitor, LXY2, was administered to mice on day 4 post-depilation.[43] Compared with the control group that received PBS, LXY2 demonstrated a significant delay in hair regrowth (Figures 7E and S7F). Consistently, the accumulation of RORγt^{fm+} cILC2s around the hair follicle DP region was also compromised (Figures 7F and 7G). To exclude potential impacts of LXY2 on hair follicle cells, we also generated reconstituted *Gata3$^{fl/fl}$VavCre* mice with cILC2s experiencing interference in *Itga3* expression. Briefly, sort-purified cILC2s were infected by lentivirus expressing short harpin RNAs for *Itga3* or the corresponding scramble sequence. Subsequently, *Gata3$^{fl/fl}$VavCre* mice reconstituted with either of the lentivirally infected cILC2s, along with T cells, underwent depilation-induced hair regrowth after 4–6 weeks (Figure 7H). The reduced expression of integrin α3β1 on the cILC2s with sh*Itga3* was validated, and the delayed hair regrowth in their reconstituted mice was recaptured (Figures 7H, S7G, and S7H).

Collectively, our data suggest a pivotal regulatory role of GATA3 in promoting integrin α3β1 expression on RORγt^{fm+} cILC2s, thereby positioning them around the hair follicle DP region to facilitate hair regrowth.

DISCUSSION

Skin ILCs exhibit varying cytokine profiles during atopic dermatitis and psoriasis, indicating their distinction from canonical ILC2s.[21,44] And, their roles in physiology remain poorly defined. Here, we observe a notable decrease in GATA3 expression in cILC2s, with a significant proportion of them diverging into RORγt^{fm+} cells. GATA3 functions in a dose-dependent manner.[36] Consistently, the decreased levels of GATA3 in cILC2s result in unique regulatory roles. Particularly, GATA3 is dispensable for the maintenance of cILC2s, as demonstrated

in tamoxifen-treated *Gata3$^{fl/fl}$CreER^{T2}* mice and *Rorc*-fm^{ΔGata3} mice. The elevated levels of *Bcl2a1* in cILC2s compared with canonical ILC2s indicate a potential role of this anti-apoptotic molecule in promoting the survival of cILC2s. However, further investigation is still required. Additionally, *Gata3* deficiency in cILC2s does not lead to reduced IL-7R expression as in ILC3s and LTi cells, which is also associated with their persistence in the skin. Moreover, although the ILC2 effector genes remain upregulated by GATA3 in cILC2s as in canonical ILC2s, the overall GATA3-upregulated genes in cILC2s are distinctive. Therefore, in line with the decreased GATA3 levels, its transcriptional regulatory roles in cILC2s differ significantly from those in canonical ILC2s.

GATA3 has been reported to suppress RORγt expression.[13] In line with this, we find a correlation between decreased GATA3 levels in cILC2s and an expansion of RORγt^{fm+} cILC2s. Although the RORγt levels in RORγt^{fm+} cILC2s are modest, these cells exhibit some characteristics resembling ILC3s, such as IL-17A production upon stimulation. We have observed a notable increase in RORγt expression in cILC2s around P14, indicating their divergence at this phase. This postnatal upregulation of RORγt may imprint certain ILC3-like features on RORγt^{fm+} cILC2s. A previous study documented the transition of skin ILCs toward a pathogenic ILC3-like state during psoriasis.[23] Our study, however, indicates that RORγt^{fm+} cILC2s already exhibit certain ILC3-like traits under steady-state conditions. It is important to note that the classification, trajectory, and characteristics of cILC2s in our study differ from those in the previous study, primarily due to differences in tissue environments. Furthermore, RORγt$^{fm−}$ cILC2s do not diverge into RORγt^{fm+} cILC2s in adulthood, suggesting that additional unidentified factors present around P14 are also necessary for initiating RORγt expression in cILC2s.

Through scRNA-seq analysis, we have identified six cILC2 clusters, with four of them displaying the RORγt^{fm+} cILC2 feature. The change in cell density along the RORγt^{fm+} cILC2 trajectory in *Gata3^{KO}* and *Rorc^{KO}* mice suggests that their divergence is orchestrated sequentially by RORγt and GATA3. Further, *Gata3* deficiency disrupts the divergency of RORγt^{fm+} cILC2s toward the terminal stage during hair follicle recycling, as indicated by their impaired CCR6 upregulation. RORγt^{fm+} cILC2s have been reported to localize around the sebaceous gland to restrict hyperplasia by producing TNF.[22] Our study reveals an additional role of RORγt^{fm+} cILC2s in facilitating hair follicle recycling. They accumulate around the hair follicle DP region on day 7 of depilation-induced hair regrowth. This positioning is also regulated by GATA3, which directly promotes *Itga3* upregulation. The enhanced terminal divergency and *Itga3* levels regulated by GATA3 may confer crucial functions to the RORγt^{fm+} cILC2s during hair follicle recycling.

It has been previously reported that Treg cells are also involved in regulating hair follicle recycling. However, Treg cells primarily accumulate around the bulge region of hair follicles

---

(H) Schematics of depilation-induced hair regrowth in *Gata3$^{fl/fl}$VavCre* mice reconstituted by T cells and RORγt^{fm+} cILC2s from *Rorc*-fm or *Rorc*-fm^{ΔGata3} mice (top), and the kinetics (*n* = 4 per group) (bottom).

Data are shown as mean ± SEM. *p* values are calculated by unpaired t test. ns, not significant, *$p < 0.05$, **$p < 0.01$, ***$p < 0.001$. Data are representative of two independent experiments (A–C and H) and at least three independent experiments (D–G).

See also Figure S6.

(legend on next page)

Developmental Cell
Article

🔂 CellPress
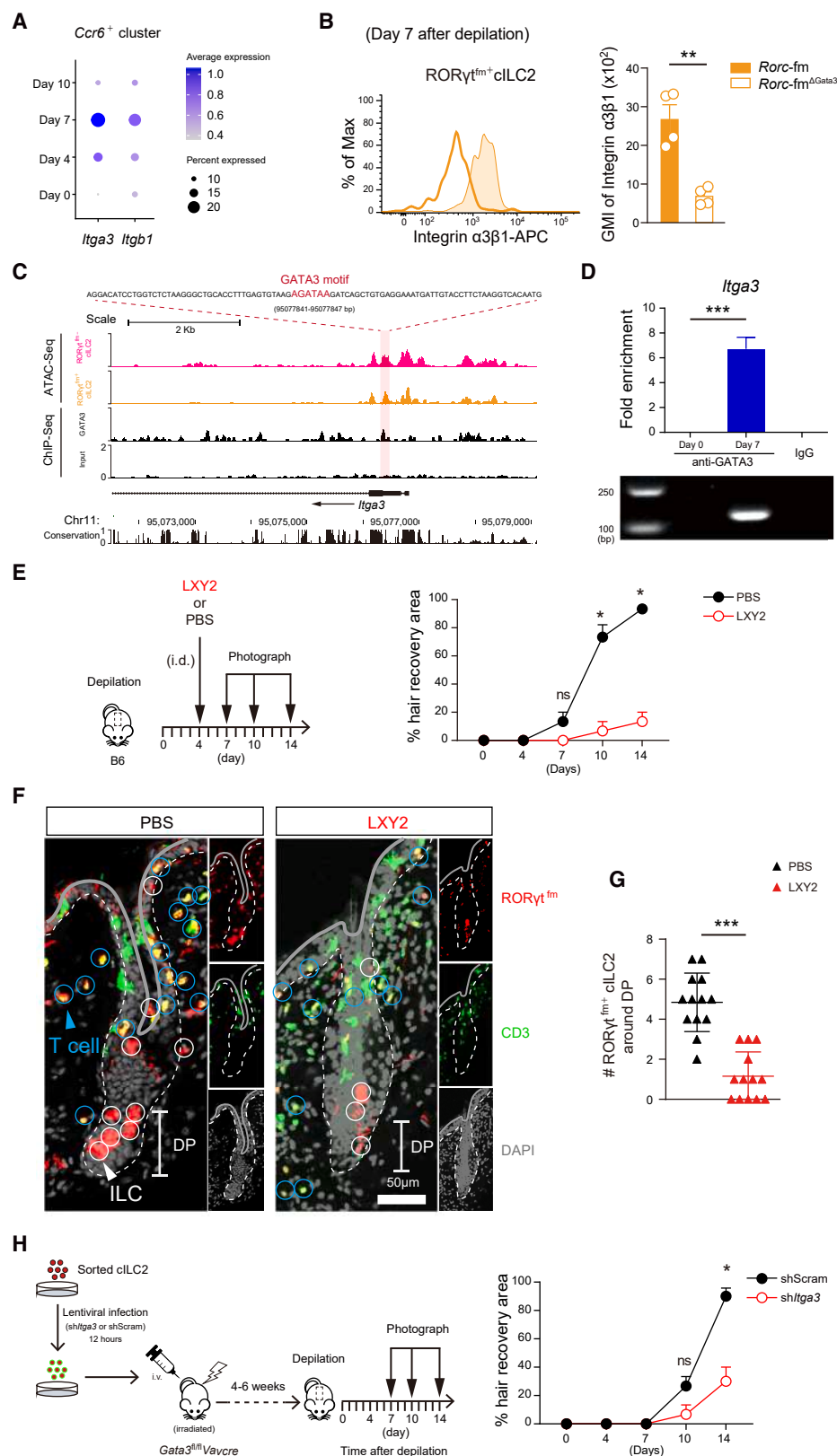
and exert their regulatory roles at a time point earlier than day 7.[19] Therefore, it appears that cILC2s and Treg cells have distinct roles during hair follicle recycling. Indeed, *Gata3*^{fl/fl}*Vav*Cre mice constituted with T cells alone are unable to fully restore depilation-induced hair regrowth. Thus, these findings further expand our knowledge of immune regulation during hair follicle recycling.

Type 2 cytokines have been reported to impair hair follicle recycling.[25] Consistently, we have observed decreased expression of *Il5* and *Il13* in the *Ccr6*^{+} cILC2s on day 7 of depilation-induced hair regrowth. By contrast, the regulatory role of GATA3 appears to be enhanced. Interestingly, we have detected increased expression of *Ostf1*, *Fgl2*, *S100a4*, *S100a6*, *S100a10*, and *S100a11* in the *Ccr6*^{+} cILC2s on day 7 post-depilation, indicating that cILC2s may perform different functions compared with canonical ILC2s during this process. These differences imply that cILC2s represent a unique subgroup within ILC2s. Despite being overlooked previously, further investigations are still necessary to fully understand the significance of cILC2s in skin physiology and pathology.

Limitations of the study

It is important to acknowledge that the use of straight gene deletion strategies to elucidate the function of GATA3 in regulating the divergence of RORγt[fm+] cILC2s and the subsequent roles of RORγt and GATA3 in sequentially promoting their further divergency toward the terminal stage may introduce potential extrinsic differences. Thus, further diligent validation may still be necessary to strengthen this conclusion.

STAR★METHODS

Detailed methods are provided in the online version of this paper and include the following:

- KEY RESOURCES TABLE
- RESOURCE AVAILABILITY
  - Lead contact
  - Materials availability
  - Data and code availability
- EXPERIMENTAL MODEL AND STUDY PARTICIPANT DETAILS
- METHOD DETAILS
  - Tamoxifen treatment
  - Tissue digestion and cell preparation
  - Cell staining, flow cytometry, and cell sorting
  - Cell culture
  - Cell transfer
  - LXY2 treatment
  - Short hairpin RNA lentiviral transduction
  - Immunofluorescent staining
  - Bulk RNA-sequencing
  - Single-cell RNA-sequencing
  - CUT&RUN qPCR
  - ATAC-sequencing
- QUANTIFICATION AND STATISTICAL ANALYSIS

SUPPLEMENTAL INFORMATION

Supplemental information can be found online at https://doi.org/10.1016/j.devcel.2024.04.015.

AUTHOR CONTRIBUTIONS

C.Z. conceived the project. G.R. performed the majority of experiments. Yime Zhang performed bulk RNA-seq and scRNA-seq analyses. J.L. performed some experiments. W.C. performed scRNA-seq analysis. D.W., M.H., and Yanyu Zhang helped with bulk RNA-seq, ATAC-seq, scRNA-seq, and CUT&RUN libraries. X.H. helped with cell sorting. X.Z., Z.H., and M.Z. helped with some experiments. L.H. and B.Z. helped with bioinformatics analysis. R.K.G. and J.Z. provided critical reagent (*Gata3*[ZsG-fl/fl] mice). W.J. provided critical advice for the project. C.Z. and G.R. wrote the manuscript. C.Z. supervised the project.

DECLARATION OF INTERESTS

The authors declare no competing interests.

Figure 7. GATA3 directs the positioning of RORγt[fm+] cILC2s via upregulating integrin α3β1

(A) Bubble plot showing the expression of *Itga3* and *Itgb1* in the *Ccr6*^{+} cluster during depilation-induced hair regrowth.

(B) Representative histogram showing integrin α3β1 expression on RORγt[fm+] cILC2s from dorsal skin of *Rorc*-fm or *Rorc*-fm[ΔGata3] mice on day 7 post-depilation (left), and GMI of the integrin α3β1 levels (*n* = 4 per group) (right).

(C) Browser tracks displaying accessible chromatin regions in RORγt[fm+] and RORγt[fm−] cILC2s and GATA3 binding sites in canonical ILC2s (GSE71198) at the *Itga3* locus.

(D) CUT&RUN-qPCR illustrating binding of GATA3 to the *Itga3* locus at the indicated site (C) on days 0 and 7 of depilation-induced hair regrowth (*n* = 4 per group). IgG is utilized as a negative control.

(E) Schematics of depilation-induced hair regrowth in *Rorc*-fm mice administered by PBS or LXY2 on day 4 (left), and the kinetics (*n* = 4 per group) (right).

(F) Representative confocal images showing the positioning of RORγt[fm+] cILC2s around hair follicles of *Rorc*-fm mice administered by PBS or LXY2 (E).

(G) Numbers of RORγt[fm+] cILC2s around hair follicle DP region on day 7 post-depilation (*n* = 13 per group). Each dot represents the number of cells around a single follicle (<20 μm).

(H) Schematics of depilation-induced hair regrowth in *Gata3*^{fl/fl}*Vav*Cre mice reconstituted with cILC2s infected by lentivirus expressing sh*Itga3* or shScram RNAs (left), and the kinetics (*n* = 4 per group) (right).

Data are shown as mean ± SEM. *p* values are calculated by unpaired t test. ns, not significant, *$p < 0.05$, **$p < 0.01$, ***$p < 0.001$. Data are representative of two independent experiments (A and C) and at least three independent experiments (B and D–H).
See also Figure S7.

REFERENCES

1. Spits, H., Artis, D., Colonna, M., Diefenbach, A., Di Santo, J.P., Eberl, G., Koyasu, S., Locksley, R.M., McKenzie, A.N.J., Mebius, R.E., et al. (2013). Innate lymphoid cells — a proposal for uniform nomenclature. Nat. Rev. Immunol. *13*, 145–149. https://doi.org/10.1038/nri3365.

2. Artis, D., and Spits, H. (2015). The biology of innate lymphoid cells. Nature *517*, 293–301. https://doi.org/10.1038/nature14189.

3. Eberl, G., Colonna, M., Di Santo, J.P., and McKenzie, A.N.J. (2015). Innate lymphoid cells. Innate lymphoid cells: a new paradigm in immunology. Science *348*, aaa6566. https://doi.org/10.1126/science.aaa6566.

4. Vivier, E., Artis, D., Colonna, M., Diefenbach, A., Di Santo, J.P., Eberl, G., Koyasu, S., Locksley, R.M., McKenzie, A.N.J., Mebius, R.E., et al. (2018). Innate lymphoid cells: 10 years on. Cell *174*, 1054–1066. https://doi.org/10.1016/j.cell.2018.07.017.

5. Constantinides, M.G., McDonald, B.D., Verhoef, P.A., and Bendelac, A. (2014). A committed precursor to innate lymphoid cells. Nature *508*, 397–401. https://doi.org/10.1038/nature13047.

6. Zhong, C., Zheng, M., Cui, K., Martins, A.J., Hu, G., Li, D., Tessarollo, L., Kozlov, S., Keller, J.R., Tsang, J.S., et al. (2020). Differential expression of the transcription factor GATA3 specifies lineage and functions of innate lymphoid cells. Immunity *52*, 83–95.e4. https://doi.org/10.1016/j.immuni.2019.12.001.

7. Sawa, S., Cherrier, M., Lochner, M., Satoh-Takayama, N., Fehling, H.J., Langa, F., Di Santo, J.P., and Eberl, G. (2010). Lineage relationship analysis of RORgammat+ innate lymphoid cells. Science *330*, 665–669. https://doi.org/10.1126/science.1194597.

8. Hoyler, T., Klose, C.S.N., Souabni, A., Turqueti-Neves, A., Pfeifer, D., Rawlins, E.L., Voehringer, D., Busslinger, M., and Diefenbach, A. (2012). The transcription factor GATA-3 controls cell fate and maintenance of type 2 innate lymphoid cells. Immunity *37*, 634–648. https://doi.org/10.1016/j.immuni.2012.06.020.

9. Yagi, R., Zhong, C., Northrup, D.L., Yu, F., Bouladoux, N., Spencer, S., Hu, G., Barron, L., Sharma, S., Nakayama, T., et al. (2014). The transcription factor GATA3 is critical for the development of all IL-7Ralpha-expressing innate lymphoid cells. Immunity *40*, 378–388. https://doi.org/10.1016/j.immuni.2014.01.012.

10. Klose, C.S.N., Flach, M., Möhle, L., Rogell, L., Hoyler, T., Ebert, K., Fabiunke, C., Pfeifer, D., Sexl, V., Fonseca-Pereira, D., et al. (2014). Differentiation of type 1 ILCs from a common progenitor to all helper-like innate lymphoid cell lineages. Cell *157*, 340–356. https://doi.org/10.1016/j.cell.2014.03.030.

11. Zhu, J. (2017). GATA3 regulates the development and functions of innate lymphoid cell subsets at multiple stages. Front. Immunol. *8*, 1571. https://doi.org/10.3389/fimmu.2017.01571.

12. Yu, Y., Tsang, J.C.H., Wang, C., Clare, S., Wang, J., Chen, X., Brandt, C., Kane, L., Campos, L.S., Lu, L., et al. (2016). Single-cell RNA-seq identifies a PD-1(hi) ILC progenitor and defines its development pathway. Nature *539*, 102–106. https://doi.org/10.1038/nature20105.

13. Zhong, C., Cui, K., Wilhelm, C., Hu, G., Mao, K., Belkaid, Y., Zhao, K., and Zhu, J. (2016). Group 3 innate lymphoid cells continuously require the transcription factor GATA-3 after commitment. Nat. Immunol. *17*, 169–178. https://doi.org/10.1038/ni.3318.

14. Klose, C.S.N., and Artis, D. (2016). Innate lymphoid cells as regulators of immunity, inflammation and tissue homeostasis. Nat. Immunol. *17*, 765–774. https://doi.org/10.1038/ni.3489.

15. Kabashima, K., Honda, T., Ginhoux, F., and Egawa, G. (2019). The immunological anatomy of the skin. Nat. Rev. Immunol. *19*, 19–30. https://doi.org/10.1038/s41577-018-0084-5.

16. Eyerich, S., Eyerich, K., Traidl-Hoffmann, C., and Biedermann, T. (2018). Cutaneous barriers and skin immunity: differentiating A connected network. Trends Immunol. *39*, 315–327. https://doi.org/10.1016/j.it.2018.02.004.

17. Kobayashi, T., Ricardo-Gonzalez, R.R., and Moro, K. (2020). Skin-resident innate lymphoid cells - cutaneous innate guardians and regulators. Trends Immunol. *41*, 100–112. https://doi.org/10.1016/j.it.2019.12.004.

18. Liu, Y., Wang, H., Taylor, M., Cook, C., Martínez-Berdeja, A., North, J.P., Harirchian, P., Hailer, A.A., Zhao, Z., Ghadially, R., et al. (2022). Classification of human chronic inflammatory skin disease based on single-cell immune profiling. Sci. Immunol. *7*, eabl9165. https://doi.org/10.1126/sciimmunol.abl9165.

19. Ali, N., Zirak, B., Rodriguez, R.S., Pauli, M.L., Truong, H.A., Lai, K., Ahn, R., Corbin, K., Lowe, M.M., Scharschmidt, T.C., et al. (2017). Regulatory T cells in skin facilitate epithelial stem cell differentiation. Cell *169*, 1119–1129.e11. https://doi.org/10.1016/j.cell.2017.05.002.

20. Liu, Z., Hu, X., Liang, Y., Yu, J., Li, H., Shokhirev, M.N., and Zheng, Y. (2022). Glucocorticoid signaling and regulatory T cells cooperate to maintain the hair-follicle stem-cell niche. Nat. Immunol. *23*, 1086–1097. https://doi.org/10.1038/s41590-022-01244-9.

21. Ricardo-Gonzalez, R.R., Van Dyken, S.J., Schneider, C., Lee, J., Nussbaum, J.C., Liang, H.E., Vaka, D., Eckalbar, W.L., Molofsky, A.B., Erle, D.J., and Locksley, R.M. (2018). Tissue signals imprint ILC2 identity with anticipatory function. Nat. Immunol. *19*, 1093–1099. https://doi.org/10.1038/s41590-018-0201-4.

22. Kobayashi, T., Voisin, B., Kim, D.Y., Kennedy, E.A., Jo, J.H., Shih, H.Y., Truong, A., Doebel, T., Sakamoto, K., Cui, C.Y., et al. (2019). Homeostatic control of sebaceous glands by innate lymphoid cells regulates commensal bacteria equilibrium. Cell *176*, 982–997.e16. https://doi.org/10.1016/j.cell.2018.12.031.

23. Bielecki, P., Riesenfeld, S.J., Hütter, J.C., Torlai Triglia, E., Kowalczyk, M.S., Ricardo-Gonzalez, R.R., Lian, M., Amezcua Vesely, M.C., Kroehling, L., Xu, H., et al. (2021). Skin-resident innate lymphoid cells converge on a pathogenic effector state. Nature *592*, 128–132. https://doi.org/10.1038/s41586-021-03188-w.

24. Sakamoto, K., Jin, S.P., Goel, S., Jo, J.H., Voisin, B., Kim, D., Nadella, V., Liang, H., Kobayashi, T., Huang, X., et al. (2021). Disruption of the endopeptidase ADAM10-Notch signaling axis leads to skin dysbiosis and innate lymphoid cell-mediated hair follicle destruction. Immunity *54*, 2321–2337.e10. https://doi.org/10.1016/j.immuni.2021.09.001.

25. Ricardo-Gonzalez, R.R., Kotas, M.E., O'Leary, C.E., Singh, K., Damsky, W., Liao, C., Arouge, E., Tenvooren, I., Marquez, D.M., Schroeder, A.W., et al. (2022). Innate type 2 immunity controls hair follicle commensalism by demodex mites. Immunity *55*, 1891–1908.e12. https://doi.org/10.1016/j.immuni.2022.08.001.

26. Kim, B.S., Siracusa, M.C., Saenz, S.A., Noti, M., Monticelli, L.A., Sonnenberg, G.F., Hepworth, M.R., Van Voorhees, A.S., Comeau, M.R., and Artis, D. (2013). TSLP elicits IL-33-independent innate lymphoid cell responses to promote skin inflammation. Sci. Transl. Med. *5*, 170ra16. https://doi.org/10.1126/scitranslmed.3005374.

27. Roediger, B., Kyle, R., Yip, K.H., Sumaria, N., Guy, T.V., Kim, B.S., Mitchell, A.J., Tay, S.S., Jain, R., Forbes-Blom, E., et al. (2013). Cutaneous immunosurveillance and regulation of inflammation by group 2 innate lymphoid cells. Nat. Immunol. *14*, 564–573. https://doi.org/10.1038/ni.2584.

28. Nussbaum, J.C., Van Dyken, S.J., von Moltke, J., Cheng, L.E., Mohapatra, A., Molofsky, A.B., Thornton, E.E., Krummel, M.F., Chawla, A., Liang, H.E., and Locksley, R.M. (2013). Type 2 innate lymphoid cells control eosinophil homeostasis. Nature *502*, 245–248. https://doi.org/10.1038/nature12526.

29. Schneider, C., Lee, J., Koga, S., Ricardo-Gonzalez, R.R., Nussbaum, J.C., Smith, L.K., Villeda, S.A., Liang, H.E., and Locksley, R.M. (2019). Tissue-resident Group 2 innate lymphoid cells differentiate by layered ontogeny and in situ perinatal priming. Immunity *50*, 1425–1438.e5. https://doi.org/10.1016/j.immuni.2019.04.019.

30. Leyva-Castillo, J.M., Galand, C., Mashiko, S., Bissonnette, R., McGurk, A., Ziegler, S.F., Dong, C., McKenzie, A.N.J., Sarfati, M., and Geha, R.S. (2020). ILC2 activation by keratinocyte-derived IL-25 drives IL-13 production at sites of allergic skin inflammation. J. Allergy Clin. Immunol. *145*, 1606–1614.e4. https://doi.org/10.1016/j.jaci.2020.02.026.

Developmental Cell
Article

CellPress

31. Schwartz, C., Moran, T., Saunders, S.P., Kaszlikowska, A., Floudas, A., Bom, J., Nunez, G., Iwakura, Y., O'Neill, L., Irvine, A.D., et al. (2019). Spontaneous atopic dermatitis in mice with a defective skin barrier is independent of ILC2 and mediated by IL-1beta. Allergy 74, 1920–1933. https://doi.org/10.1111/all.13801.

32. Salimi, M., Barlow, J.L., Saunders, S.P., Xue, L., Gutowska-Owsiak, D., Wang, X., Huang, L.C., Johnson, D., Scanlon, S.T., McKenzie, A.N.J., et al. (2013). A role for IL-25 and IL-33-driven type-2 innate lymphoid cells in atopic dermatitis. J. Exp. Med. 210, 2939–2950. https://doi.org/10.1084/jem.20130351.

33. Zeis, P., Lian, M., Fan, X., Herman, J.S., Hernandez, D.C., Gentek, R., Elias, S., Symowski, C., Knöpper, K., Peltokangas, N., et al. (2020). In situ maturation and tissue adaptation of Type 2 innate lymphoid cell progenitors. Immunity 53, 775–792.e9. https://doi.org/10.1016/j.immuni.2020.09.002.

34. Gurram, R.K., Wei, D., Yu, Q., Kamenyeva, O., Chung, H., Zheng, M., Butcher, M.J., Kabat, J., Liu, C., Khillan, J.S., and Zhu, J. (2022). Gata3 (ZsG) and Gata3 (ZsG-fl): novel murine Gata3 reporter alleles for identifying and studying Th2 cells and ILC2s in vivo. Front. Immunol. 13, 975958. https://doi.org/10.3389/fimmu.2022.975958.

35. Shih, H.Y., Sciumè, G., Mikami, Y., Guo, L., Sun, H.W., Brooks, S.R., Urban, J.F., Jr., Davis, F.P., Kanno, Y., and O'Shea, J.J. (2016). Developmental acquisition of Regulomes underlies innate lymphoid cell functionality. Cell 165, 1120–1133. https://doi.org/10.1016/j.cell.2016.04.029.

36. Klein Wolterink, R.G.J., Serafini, N., van Nimwegen, M., Vosshenrich, C.A.J., de Bruijn, M.J.W., Fonseca Pereira, D., Veiga Fernandes, H., Hendriks, R.W., and Di Santo, J.P. (2013). Essential, dose-dependent role for the transcription factor Gata3 in the development of IL-5+ and IL-13+ type 2 innate lymphoid cells. Proc. Natl. Acad. Sci. USA 110, 10240–10245. https://doi.org/10.1073/pnas.1217158110.

37. Vogler, M. (2012). BCL2A1: the underdog in the BCL2 family. Cell Death Differ. 19, 67–74. https://doi.org/10.1038/cdd.2011.158.

38. Lionnard, L., Duc, P., Brennan, M.S., Kueh, A.J., Pal, M., Guardia, F., Mojsa, B., Damiano, M.A., Mora, S., Lassot, I., et al. (2019). TRIM17 and TRIM28 antagonistically regulate the ubiquitination and anti-apoptotic activity of BCL2A1. Cell Death Differ. 26, 902–917. https://doi.org/10.1038/s41418-018-0169-5.

39. Dann, E., Henderson, N.C., Teichmann, S.A., Morgan, M.D., and Marioni, J.C. (2022). Differential abundance testing on single-cell data using k-nearest neighbor graphs. Nat. Biotechnol. 40, 245–253. https://doi.org/10.1038/s41587-021-01033-z.

40. Arimori, T., Miyazaki, N., Mihara, E., Takizawa, M., Taniguchi, Y., Cabañas, C., Sekiguchi, K., and Takagi, J. (2021). Structural mechanism of laminin recognition by integrin. Nat. Commun. 12, 4012. https://doi.org/10.1038/s41467-021-24184-8.

41. DeRouen, M.C., Zhen, H., Tan, S.H., Williams, S., Marinkovich, M.P., and Oro, A.E. (2010). Laminin-511 and integrin beta-1 in hair follicle development and basal cell carcinoma formation. BMC Dev. Biol. 10, 112. https://doi.org/10.1186/1471-213X-10-112.

42. Tayem, R., Niemann, C., Pesch, M., Morgner, J., Niessen, C.M., Wickström, S.A., and Aumailley, M. (2021). Laminin 332 is indispensable for homeostatic epidermal differentiation programs. J. Invest. Dermatol. 141, 2602–2610.e3. https://doi.org/10.1016/j.jid.2021.04.008.

43. Yao, N., Xiao, W., Wang, X., Marik, J., Park, S.H., Takada, Y., and Lam, K.S. (2009). Discovery of targeting ligands for breast cancer cells using the one-bead one-compound combinatorial method. J. Med. Chem. 52, 126–133. https://doi.org/10.1021/jm801062d.

44. Bernink, J.H., Ohne, Y., Teunissen, M.B.M., Wang, J., Wu, J., Krabbendam, L., Guntermann, C., Volckmann, R., Koster, J., van Tol, S., et al. (2019). c-Kit-positive ILC2s exhibit an ILC3-like signature that may contribute to IL-17-mediated pathologies. Nat. Immunol. 20, 992–1003. https://doi.org/10.1038/s41590-019-0423-0.

45. Xu, M., Lu, H., Lee, Y.H., Wu, Y., Liu, K., Shi, Y., An, H., Zhang, J., Wang, X., Lai, Y., and Dong, C. (2018). An interleukin-25-mediated autoregulatory circuit in keratinocytes plays a pivotal role in psoriatic skin inflammation. Immunity 48, 787–798.e4. https://doi.org/10.1016/j.immuni.2018.03.019.

46. Wu, D., Hu, L., Han, M., Deng, Y., Zhang, Y., Ren, G., Zhao, X., Li, Z., Li, P., Zhang, Y., et al. (2022). PD-1 signaling facilitates activation of lymphoid tissue inducer cells by restraining fatty acid oxidation. Nat. Metab. 4, 867–882. https://doi.org/10.1038/s42255-022-00595-9.

47. Sachs, N., Secades, P., van Hulst, L., Kreft, M., Song, J.Y., and Sonnenberg, A. (2012). Loss of integrin alpha3 prevents skin tumor formation by promoting epidermal turnover and depletion of slow-cycling cells. Proc. Natl. Acad. Sci. USA 109, 21468–21473. https://doi.org/10.1073/pnas.1204614110.

STAR★METHODS

KEY RESOURCES TABLE

REAGENT or RESOURCE	SOURCE	IDENTIFIER
Antibodies		
eFluor™ 450 anti-mouse CD3e (Clone 145-2C-11)	eBioscience	Cat#48-0031-82; RRID: AB_10735092
eFluor™ 450 anti-mouse CD19 (Clone eBio1D3)	eBioscience	Cat#48-0193; RRID: AB_2043815
eFluor™ 450 anti-mouse CD5 (Clone 53-7.3)	eBioscience	Cat#48-0051-82; RRID: AB_1603250
eFluor™ 450 anti-mouse Ly-6G/Ly-6C(Gr-1) (Clone RB6-8C5)	eBioscience	Cat#48-5931-82; RRID: AB_1548788
eFluor™ 450 anti-mouse CD11b (Clone M1/70)	eBioscience	Cat#48-0112-82; RRID: AB_1582236
eFluor™ 450 anti-mouse CD11c (Clone N418)	eBioscience	Cat#48-0114-82; RRID: AB_1548654
eFluor™ 450 anti-mouse NK1.1 (Clone PK136)	eBioscience	Cat#48-5941-82; RRID: AB_2043877
eFluor™ 450 anti-mouse TER119 (Clone TER-119)	eBioscience	Cat#48-5921-82; RRID: AB_1518808
eFluor™ 450 anti-mouse CD45R(B220) (Clone RA3-6B2)	eBioscience	Cat#48-0452-82; RRID: AB_1548761
PE-Cyanine7 anti-mouse CD127(Clone A7R34)	eBioscience	Cat#25-1271-82; RRID: AB_469649
APC-Cyanine7 anti-mouse CD90.2(Clone 30-H12)	Biolegend	Cat#105328; RRID: AB_10613280
Super Bright™ 645 anti-mouse CD4(Clone RM4-5)	eBioscience	Cat#64-0042-82; RRID: AB_2662401
Brilliant Violet 650™ anti-mouse CD45.1(Clone A20)	Biolegend	Cat#110736; RRID: AB_11124743
Brilliant Violet 650™ anti-mouse CD179(c-Kit) (Clone ACK2)	Biolegend	Cat#135125; RRID: AB_2562446
Brilliant Violet 785™ anti-mouse CD196(CCR6) (Clone 29-2L17)	Biolegend	Cat#129823; RRID: AB_2715923
Brilliant Violet 785™ anti-mouse CD127(IL-7Ra) (Clone A7R34)	Biolegend	Cat#135037; RRID: AB_2565269
Brilliant Violet 785™ anti-mouse CD25(Clone PC61)	Biolegend	Cat#102051; RRID: AB_2564131
Brilliant Violet 785™ anti-mouse CD45.2(Clone 104)	Biolegend	Cat#109839; RRID: AB_2562604
FITC anti-mouse CD3e (Clone 145-2C11)	Biolegend	Cat#100306; RRID: AB_312671
FITC anti-mouse NK1.1(Clone PK136)	Biolegend	Cat#108706; RRID: AB_313392
FITC anti-mouse TER119(Clone TER-119)	Biolegend	Cat#116206; RRID: AB_313707
FITC anti-mouse CD5(Clone 53-7.3)	Biolegend	Cat#100606; RRID: AB_312735
FITC anti-mouse CD19(Clone 6D5)	Biolegend	Cat#115506; RRID: AB_313640
FITC anti-mouse Ly-6G/Ly-6C(Gr-1) (Clone RB6-8C5)	Biolegend	Cat#108406; RRID: AB_313370
FITC anti-mouse/human CD11b (Clone M1/70)	Biolegend	Cat#101206; RRID: AB_312788
FITC anti-mouse CD11c (Clone N418)	Biolegend	Cat#117306; RRID: AB_313775
FITC anti-mouse CD45.2(Clone 104)	Biolegend	Cat#109806; RRID: AB_313442
FITC anti-mouse CD45RB(B220) (Clone RA3-6B2)	Biolegend	Cat#103206; RRID: AB_312991
BD Horizon™ BV650 anti-mouse T-bet (Clone 04-46)	BD Biosciences	Cat#564142; RRID: AB_2738616
BD Pharmingen™ Alexa Fluor® 488 anti-mouse GATA3(Clone L50-823)	BD Biosciences	Cat#560077; RRID: AB_1645303
BD Horizon™ PE-CF594 anti-mouse RORγt (Clone Q31-378)	BD Biosciences	Cat#562684; RRID: AB_2651150
BD Pharmingen™ PE-Cy™7 anti-mouse GATA3(L50-823)	BD Biosciences	Cat#560405; RRID: AB_1645544
BD Pharmingen™ Alexa Fluor® 647 anti-mouse T-bet (Clone O4-46)	BD Biosciences	Cat#561267; RRID: AB_10564093

(Continued on next page)

Developmental Cell
Article

CellPress

Continued

REAGENT or RESOURCE	SOURCE	IDENTIFIER
PE FOXP3 Monoclonal antibody (Clone FJK-16s)	eBioscience	Cat#12-5773-82; RRID: AB_465936
PE-Cyanine7 FOXP3 Monoclonal antibody (Clone FJK-16s)	eBioscience	Cat#25-5773-82; RRID: AB_891552
PE anti-mouse CD45.2	Biolegend	Cat#109808; RRID: AB_313445
Rat anti-mouse CD16/32	Biolegend	Cat#101320; RRID: AB_1574973
APC Rat anti-Integrinα3+β1 polyclonal antibody (Clone 976-1025/35-47)	BIOSS	Cat#bs-1057R; RRID: AB_10856085
PE anti-mouse TCR γ/δ (Clone GL3)	Biolegend	Cat#118108; RRID: AB_313832
APC-eFluor™ 780 anti-mouse CD45(Clone 30-F11)	eBioscience	Cat#47-0451-82; RRID: AB_1548781
PE anti-mouse CD196 (CCR6) (Clone 29-2L17)	Biolegend	Cat#129804; RRID: AB_1279139
PE-Cyanine7 anti-mouse IL-17A (Clone TC11-18H10.1)	Biolegend	Cat#506922; RRID: AB_2125010
FITC anti-mouse CD3(Clone 17A2)	Biolegend	Cat#100203; RRID: AB_312660
PE anti-mouse CD3(Clone 17A2)	Biolegend	Cat#100205; RRID: AB_312662
APC anti-mouse T-bet (Clone 4B10)	eBioscience	Cat#17-5825-82; RRID: AB_2744712
FITC anti-mouse/human KLRG1(Clone 2F1/KLRG1)	Biolegend	Cat#138410; RRID: AB_10643998
APC-Cyanine7 anti-mouse/human KLRG1(Clone 2F1/KLRG1)	Biolegend	Cat#138425; RRID: AB_2566553
PE anti-mouse CD218a(IL-18Ra) (Clone P3TUNYA)	eBioscience	Cat#12-5183-82; RRID: AB_2572617
APC anti-mouse CD218a(IL-18Ra) (Clone A17071D)	Biolegend	Cat#157906; RRID: AB_2860735
PE/Cyanine7 anti-mouse IL-33Rα (IL1RL1, ST2) (Clone DIH9)	Biolegend	Cat#145315; RRID: AB_2687366
Biotin anti-mouse IL-33Rα (IL1RL1, ST2) (Clone DJ8)	MD Biosciences	Cat#101001B; RRID: AB_947551
Alexa Fluor™ 700 anti-mouse CD103(Clone 2E7)	eBioscience	Cat#56-1031-82; RRID: AB_2637111
Brilliant Violet 421™ anti-mouse/human IL-5(Clone TRFK5)	Biolegend	Cat#504311; RRID: AB_2563161
eFluor™ 660 anti-mouse IL-13(Clone eBio13A)	eBioscience	Cat#50-7133-82; RRID: AB_2574279
APC anti-mouse CD8b (Clone H35-17.2)	eBioscience	Cat#17-0083-81; RRID: AB_657760
PE anti-mouse/human CD44(Clone IM7)	Biolegend	Cat#103008; RRID: AB_493687
APC-Cyanine7 anti-mouse CD62L (Clone MEL-14)	Biolegend	Cat#104428; RRID: AB_830799
APC anti-mouse CD133(Clone 315-2C11)	Biolegend	Cat#141207; RRID: AB_10898121
BD Pharmingen™ Purified Mouse anti-GATA3(Clone L50-823)	BD Biosciences	Cat#558686; RRID: AB_2108590
BD Horizon™ BUV737 Streptavidin	BD Biosciences	Cat#564293; RRID: AB_2869560
Chemicals, peptides, and recombinant proteins		
Recombinant Human IL-2	Peprotech	Cat#200-2
Recombinant Murine IL-7	Peprotech	Cat#217-17
DNase I	Roche	Cat#10104159001
Collagenase P	Roche	Cat#11213865001
Collagenase IV	Sigma-Aldrich	Cat#C5138

(Continued on next page)

Continued

REAGENT or RESOURCE	SOURCE	IDENTIFIER
Hyaluronidase	Harveybio	Cat#EZ2176
LXY2	Chinapeptides	N/A
Foxp3/Transcription Factor Staining Buffer Set	eBioscience	Cat#00-5523-00
Paraformaldehyde	Sigma-Aldrich	Cat#P6148
Tissue-Tek® O.C.T. Compound	Sakura	Cat#4583
Neutral Protease (Dispase)	BioRuler	Cat#RH73624-25G
RPMI 1640	Gibco	Cat#31800105
Bovine serum albumin, fraction V	Sangon	Cat#A500023-0100
Triton X-100	VWR	Cat#0694-1L
Penicillin-Streptomycin	Gibco	Cat#15140-122
4-Hydroxytamoxifen, 99%	Macklin	Cat#A872541-5mg
Fetal Bovine Serum	Gibco	Cat#10099141C
Tween-20	VWR	Cat#0777-1L
eBioscience™ Cell Stimulation Cocktail (500X)	Invitrogen	Cat#00-4970-93
eBioscience™ Monensin Solution (1000X)	Invitrogen	Cat#00-4505-51
DTT	BBI	Cat#A620058
DAPI Stain Solution	BBI	Cat#E607303
eBioscience™ Fixable Viability Dye eFluor™ 506	Invitrogen	Cat#65-0866-14
Critical commercial assays		
Single Cell Full Length mRNA Amplification Kit	Vazyme	Cat#N712
TruePrep DNA Library Prep Kit V2 for Illumina	Vazyme	Cat#TD501
BD™ Mouse Immune Single-Cell Multiplexing Kit	BD Biosciences	Cat#633793
Hyperactive pG-MNase CUT&RUN Assay Kit for Illumina	Vazyme	Cat#HD102
Deposited data		
Raw data of RNA-seq and ATAC-seq	This paper	GSA: CRA010739
RNA-seq data of GATA3 sufficient and deficient ILC2	Yagi et al.[9]	GEO: GSE47851
RNA-seq data of GATA3 sufficient and deficient ILC3	Zhong et al.[13]	GEO: GSE71198
ATAC-seq data of canonical ILC2 and ILC3	Shih et al.[35]	GEO: GSE77695
Experimental models: Organisms/strains		
Mouse: Gata3 fl/fl	NIAID –Taconic repository	Line 355; PMID:15475959
Mouse: Gata3 ZsG-fl/fl	Dr. JInfang Zhu, NIAID, NIH	PMID: 36466899
Mouse: Gata3 fl/fl VavCre	NIAID –Taconic repository	Line 8446; PMID:15475959
Mouse: Id2-YFP	Dr. Jonathan R. Keller, NCI, NIH	PMID: 25051963
Mouse: Rorc-Cre	The Jackson Laboratory	Cat#JAX: 022791; RRID: IMSR_JAX:022791
Mouse: Rosa26 TdTamato	The Jackson Laboratory	Cat#JAX: 007914; RRID: IMSR_JAX:007914
Mouse: CD45.2 Rag2 −/− Il2rg −/−	The Jackson Laboratory	Cat#JAX: 014593; RRID: IMSR_JAX:014593
Mouse: Rag2 −/−	The Jackson Laboratory	Cat#JAX: 008449; RRID: IMSR_JAX:008449
Mouse: Il22 Cre	The Jackson Laboratory	Cat#JAX: 027524; RRID: IMSR_JAX:027524
Mouse: Il5 iCre	The Jackson Laboratory	Cat#JAX: 030926; RRID: IMSR_JAX:030926
Mouse: Rosa26 YFP	The Jackson Laboratory	Cat#JAX: 006148; RRID: IMSR_JAX:006148
Mouse: Rorc fl/fl	The Jackson Laboratory	Cat#JAX: 008771; RRID: IMSR_JAX:008771
Mouse: CreER^T2	The Jackson Laboratory	Cat#JAX: 007001; RRID: IMSR_JAX:007001
Mouse: C57BL/6	Department of Laboratory Animal Science, PKUHSC	N/A
Mouse: B6. CD45.1	Department of Laboratory Animal Science, PKUHSC	N/A
Software and algorithms		
FlowJo v10	Tree Star	http://www.flowjo.com/
GraphPad Prism 7	GraphPad	http://www.graphpad.com/
ImageJ	NIH	https://imagej.net/

Developmental Cell
Article

CellPress

RESOURCE AVAILABILITY

Lead contact
Further information and requests for resources and reagents should be directed to and will be fulfilled by the lead contact, Chao Zhong (zhongc@pku.edu.cn).

Materials availability
This study did not generate new unique reagents.

Data and code availability
- All data reported in this paper will be shared by the lead contact upon request.
- RNA sequencing and ATAC sequencing experiments are deposited at GSA with accession number GSA: CRA010739.
- This paper does not report original code.
- Any additional information required to reanalyze the data reported in this paper is available from the lead contact upon request.

EXPERIMENTAL MODEL AND STUDY PARTICIPANT DETAILS

All animal study protocols used for experiments were approved by the ethics committee of Peking University Health Science Center. All animals were bred and maintained in a specific-pathogen-free facility with a 12 h light/12 h dark cycle, an ambient temperature of 20-24 °C, and humidity of 30-70%. All mice used in experiments were age and sex matched. Male and female mice aged 8-16 weeks if not specifically described were used for all studies. C57BL/6 and CD45.1$^+$ congenic mice were purchased from the Department of Laboratory Animal Science, Peking University Health Science Center. $Rorc$$^{fl/fl}$, Rag2$^{-/-}$ and $Rag2$$^{-/-}$$Il2rg$$^{-/-}$ mice were purchased from the Jackson Laboratory (stock# 008771, 008449, 014593). $Gata3$$^{fl/fl}$, $Gata3$$^{fl/fl}$$Vav$Cre, $Gata3$$^{ZsG-fl/fl}$, $Gata3$$^{fl/fl}$CreER^{T2}, $Id2$$^{YFP/+}$, RORγt-fm ($Rorc$Cre-Rosa26^{TdTomato}) and RORγt-fm^{ΔGata3} ($Gata3$$^{fl/fl}$$Rorc$Cre-Rosa26^{TdTomato}) mice on C57BL/6 background were previously described.[6,9,13,34] $Gata3$$^{ZsG-fl/fl}$ mice were bred with CreER^{T2} mice (from the Jackson Laboratory, stock# 007001) to generate $Gata3$$^{ZsG-fl/fl}$CreER^{T2} mice. $Rorc$$^{fl/fl}$ mice were bred with VavCre mice to generate $Rorc$^{KO} ($Rorc$$^{fl/fl}$$Vav$Cre) mice.

METHOD DETAILS

Tamoxifen treatment
1 mg tamoxifen was dissolved in 150 ml corn oil and intraperitoneally injected into $Gata3$$^{ZsG-fl/fl}$CreER^{T2} and $Gata3$$^{fl/fl}$CreER^{T2} mice daily for five days to generate $Gata3$$^{ZsG-KO}$ and $Gata3$^{KO} mice.

Tissue digestion and cell preparation
Skin cell suspensions were prepared from mouse dorsal skin or ear, as previously described with minor modifications.[45] Briefly, for dorsal skin digestion, dorsal hairs were firstly shaved and depilated. Subcutis was teared directly, and epidermis and dermis were separated with forceps after incubating in PBS containing 25 mg/mL Dispase. The subcutis, epidermis, and dermis were cut into ∼ 2 mm X 2 mm pieces and digested in RPMI 1640 containing 1 mg/mL Collagenase P, 0.5 mg/mL Hyaluronidase and 0.1 mg/mL DNase I. For ear digestion, the dorsal and ventral sides were teared with forceps, cut into small pieces, and digested in the same condition as dorsal skin.

Digestion of small intestine was described previously.[46] Briefly, contents of small intestines were firstly emptied. Then, small intestines were opened longitudinally, cut into 1 cm length pieces, and incubated in RPMI 1640 containing 2% FBS, 5 mM EDTA and 1 mM DTT. Afterwards, the samples were vortexed three times in RPMI 1640 containing 2 mM EDTA to remove epithelial cells. The remained fragments were digested in RPMI 1640 containing 0.05 mg/ml Collagenase IV, 0.5 mg/ml Dispase and 0.1 mg/ml DNase I.

The digested cells were filtered by a 40 μm strainer, centrifugated and resuspended in PBS containing 2% FBS.

Cell staining, flow cytometry, and cell sorting
Digested cells were incubated with an anti-CD16/32 antibody first to block Fc receptors, and then stained with antibodies to surface molecules and fixable viability dye for 30 min at 4 °C. For transcription factor staining, the cells were fixed and permeabilized with the Foxp3/Transcription Factor Staining Buffer Set (eBioscience), and then transcription factors were stained for at least 4 hours at 4 °C. For intracellular cytokine staining, digested cells were resuspended in RPMI 1640 containing 10% FBS and 10 ng/mL recombinant murine IL-7, and stimulated with 50 ng/mL phorbol myristate acetate (PMA) and 500 ng/mL ionomycin for 3 hours at 37 °C, with monensin (eBioscience) added after the first 30 min. The cells were harvested and stained by antibodies to surface molecules. Then, they were fixed by 2% paraformaldehyde in PBS for 20 min at room temperature. The fixed cells were permeabilized with 0.1% triton X-100 for 10 min at room temperature, and subjected to cytokine staining for 30 min at 4 °C.

Flow cytometry were performed on LSR Fortessa (BD Biosciences), and results were analyzed by FlowJo software (FlowJo, LLC). Cell sorting was performed on Aria III cytometers (BD Biosciences) at high purity.

Antibodies specific to mouse CD3e (145-2C11), CD5 (53-7.3), CD19 (eBio1D3), B220 (RA3-6B2), Gr-1 (RB6-8C5) and CD45.2 (104) were purchased from eBioscience; antibodies specific to mouse CD127 (A7R34), CCR6 (29-2L17), CD90.2(30-H12), KLRG1 (2F1/KLRG1) and TCRγ/δ (GL3) were purchased from Biolegend; antibodies specific to mouse RORγt (Q31-378) and GATA-3 (L50-823) were purchased from BD Biosciences; antibody specific to integrin α3β1 (BS-1057R) was purchased from Bioss.

Cell culture
Sort-purified cutaneous ILC2s and siLP ILC2s were cultured in RPMI 1640 containing 10% FBS, 1X Penicillin-Streptomycin, 10 ng/mL recombinant murine IL-7 and 10 ng/mL recombinant human IL-2. To induce *Gata3* deletion *in vitro*, cutaneous ILC2s or siLP ILC2s were sort-purified from *Gata3*$^{ZsG-fl/fl}$, *Gata3*$^{ZsG-fl/fl}$CreER^{T2}, and WT CD45.1 mice. *Gata3*$^{ZsG-fl/fl}$ or *Gata3*$^{ZsG-fl/fl}$CreER^{T2} cells were mixed with CD45.1 cells at 1:1 ratio, and cultured in RPMI 1640 containing 10% FBS, 1X Penicillin-Streptomycin, 10 ng/mL recombinant murine IL-7 and 10 ng/mL recombinant human IL-2. 100 nM 4-OHT was added into the culture medium to induce *Gata3* deletion. Cells were harvested daily for flow cytometry analysis.

Cell transfer
5×10^3 cILC2s from freshly digested skin and 5×10^6 T cells from lymph nodes were sort-purified, and transferred to irradiated Gata3$^{fl/fl}$*Vav*Cre recipient mice through intravenous injection. After 4-6 weeks, depilation-induced hair follicle recycling was performed using the reconstituted mice.

LXY2 treatment
LXY2 was previously reported as a high-affinity binding ligand of integrin α3β1, inhibiting its interaction with laminin. Its structure can reference from the initial study.[43] This compound was synthesized by the company ChinaPeptides Co., Ltd. (QYAOBIO), and its quality was confirmed through mass-spectrum. To prepare this integrin α3β1 inhibitor for use, it was dissolved in PBS. On day 4 post-depilation, it was intracutaneously injected into the mice at 100 nmol per mouse.

Short hairpin RNA lentiviral transduction
Itga3 shRNA sequence (CGGATGGACATTTCAGAGAAA) described previously was cloned to pLKO.1 for lentiviral packaging.[47] Regarding the lentiviral packaging, lentiviruses containing either shScram or sh*Itga3* were generated by transfecting 293T cells in a 10 cm dish with lentiviral packaging vectors. The supernatant containing the lentivirus was collected at 48 and 72 hours post-transfection. Subsequently, the lentiviral supernatant underwent ultracentrifugation, and the resulting lentiviral pellets were resuspended in 500 μl RPMI 1640. For the lentiviral infection of cILC2s, we sort-purified 50,000 cILC2s from 6∼8 mice. These cells were then seeded into two single wells of a 96-well plate in RPMI 1640 medium supplemented with 10% fetal bovine serum (FBS) and 10 ng/ml IL-7. At the same time, 100 μl of either shScram or sh*Itga3* lentivirus was added to the well. The infection lasted for 12 hours. Subsequently, the lentivirus-infected cILC2s were harvested, washed, and resuspended in PBS. A total of 5000 cILC2s in 200 μl PBS were then intravenously injected into the recipient mice. The reconstituted mice were used for further analysis after 4-6 weeks.

Immunofluorescent staining
Skin sheets were fixed in 1% paraformaldehyde for 1 hour at room temperature, and dehydrated serially in 20% and 30% sucrose. The dehydrated samples were embedded in OCT (Tissue-Tek) and subjected to snap-freezing. Then, they were cryo-sectioned at 20 μm thickness for immunofluorescent staining. The sectioned sample was incubated in blocking buffer (0.5% BSA, 5% mouse serum and 0.1% Triton-X100) overnight at 4 °C, followed by staining with fluorescein-labeled anti-CD3 (145-2C11) and anti-45.2 (104) antibodies for 12 h at 4 °C. Afterwards, the sample was washed three times in PBS containing 0.1% tween-20. Tissue imaging was performed on Nikon N-STORM 4.0 confocal microscope (Nikon Instruments, Inc.) and analyzed using ImageJ software (NIH).

Bulk RNA-sequencing
RNA-seq library preparation was performed using Single Cell Full Length mRNA Amplification Kit (Vazyme Biotech Co., Ltd.) according to the manufacturer's instruction. Briefly, cutaneous ILC2s were collected by sorting directly to the lysis buffer for cDNAs reverse transcription and amplification using Single Cell Full Length mRNA Amplification Kit (Vazyme Biotech Co., Ltd.). RNA-seq library was prepared using TruePrep DNA Library Prep Kit V2 for Illumina (Vazyme Biotech Co., Ltd.) according to the manufacturer's instruction. Library sequencing was performed on Illumina NovaSeq platform with paired-end 150 bp reads.

The RNA-seq reads were aligned to the GRCm38/mm10 assembly of mouse genome using HISAT2, and quantified by featurecounts. Genes with confirmative expression (TPM > 5 in each repeat of any group) were used for further analysis. Differential gene expression analysis was performed by DESeq2 pipeline.

Single-cell RNA-sequencing
Sort-purified cILC2s with different genotype or at different depilation days were labelled with Sample Tags from BD™ Mouse Immune Single-Cell Multiplexing Kit (BD Biosciences), according to the manufacturer's instructions. Briefly, the BD™ Mouse Immune Single-Cell Multiplexing Kit (Cat# 633793) including Sample Tags composed of unique combinations of nuclear oligos that are conjugated to the anti-mouse CD45 antibody (Clone 30-F11) was used. Each cell sample was labeled with a unique Sample Tag and combined

Developmental Cell
Article

ℰ **CellPress**

together for subsequent single-cell capture and cDNA synthesis on BD Rhapsody Single-Cell Analysis System (BD). After library preparation, samples were sequenced on Illumina platform with paired-end 150 bp reads.

Single-cell RNA-sequencing data were aligned and quantified using BD Rhapsody WTA Local bioinformatics pipeline (version 1.9.1, BD) against the mouse GRCm38/mm10 reference genome. Quality of scRNA-seq data was assessed based on three metrics: (1) the UMI counts per cell should be less than 6000; (2) features per cell should be more than 500 and less than 2000; (3) proportion of mitochondrial genes should be less than 15%. Seurat R package was used for normalization, dimension reduction, clustering, cluster-specific marker genes identification and clusters annotation.

For demultiplexing the tagged cells and assign them to each samples, the BD Rhapsody Analysis Pipeline, as outlined in the BD® Single-Cell Multiomics Bioinformatics Handbook (Doc ID: 23–21713), was employed. This pipeline automatically integrated the Sample Tag sequences into the FASTA reference file. Consequently, reads that aligned to a particular Sample Tag were used to determine the corresponding sample.

Finally, Monocle2 was used for trajectory inference. AddModuleScore was used to score RORγt^{fm+} and RORγt^{fm-} gene signatures, and GATA3 upregulated gene signature.

CUT&RUN qPCR

CUT&RUN were performed using the Hyperactive pG-MNase CUT&RUN Assay Kit for Illumina (HD102, Vazyme Biotech Co., Ltd.) following the manufacturer's instruction. Briefly, cILC2s were sort-purified, and 1% of the cells were saved for extraction of the input genome DNA. The remaining cILC2s were then washed and permeabilized with digitonin. Next, the cells were incubated with either IgG or anti-GATA3 antibody (558686, BD Bioscience) overnight at 4°C, followed by incubation with protein G-MNase for 1 hour at 4°C.The CUT&RUN reaction was initiated by adding Ca^{2+} and lasted for 30 minutes at 0°C. Afterward, the DNA fragments released into the supernatant were extracted using phenol-chloroform. Subsequently, the DNA fragments, including the input DNA, were quantified by PCR. Primers for *Itga3*, forward 5'-TCATTCTGTGTCTGATTCCCTATCT-3', reverse 5'-TGTCAGTAATTGTCATGAG CAAAAG-3'. The relative quantification of each sample was calculated by comparing the intensity of the gel bands obtained from the CUT&RUN and input samples.

ATAC-sequencing

Sort-purified cILC2s were resuspended in 50 μL lysis buffer containing10 mM Tris-HCl pH 7.4, 10 mM NaCl, 3 mM MgCl$_2$ and 0.1% NP-40. After loading on ice for 3 minutes, the cells were centrifuged at 600 Xg for 10 min to collect nuclei. Nuclei were resuspended using transposition reaction buffer. DNA fragmentation and library preparation were performed using TruePrep DNA Library Prep Kit V2 for Illumina (Vazyme) according to the manufacturer's instruction. Quantity and quality of libraries were assessed on Agilent 2100 Bioanalyzer system. Library sequencing was performed at paired-end 150 bp on Illumina NovaSeq platform.

QUANTIFICATION AND STATISTICAL ANALYSIS

Animals were randomly allocated into different groups. Descriptive statistics were provided in the figure legends. All samples were compared using Prism v7 software (GraphPad) by either a two-sided unpaired Student's t-test. P value < 0.05 was considered as significant.